ACS APPLIED MATERIALS & INTERFACES

www.acsami.org

Research Article

Spiky Silver–Iron Oxide Nanohybrid for Effective Dual-Imaging and Synergistic Thermo-Chemotherapy

Shehzahdi S. Moonshi, Karla X. Vazquez-Prada, Joyce Tang, Nicholas J. Westra van Holthe, Gary Cowin, Yuao Wu, Huong D. N. Tran, Ryan Mckinnon, Andrew C. Bulmer, and Hang Thu Ta*

Cite This: *ACS Appl. Mater. Interfaces* 2023, 15, 42153–42169

Read Online

ACCESS | Metrics & More | Article Recommendations | Supporting Information

ABSTRACT: Nanophotothermal therapy based on nanoparticles (NPs) that convert near-infrared (NIR) light to generate heat to selectively kill cancer cells has attracted immense interest due to its high efficacy and being free of ionizing radiation damage. Here, for the first time, we have designed a novel nanohybrid, silver–iron oxide NP (AgIONP), which was successfully tuned for strong absorbance at NIR wavelengths to be effective in photothermal treatment and dual-imaging strategy using MRI and photoacoustic imaging (PAI) in a cancer model in vivo and in vitro, respectively. We strategically combine the inherent anticancer activity of silver and photothermal therapy to render excellent therapeutic capability of AgIONPs. In vitro phantoms and in vivo imaging studies displayed preferential uptake of folate-targeted NPs in a cancer mice model, indicating the selective targeting efficiency of NPs. Importantly, a single intravenous injection of NPs in a cancer mice model resulted in significant tumor reduction, and photothermal laser resulted in a further substantial synergistic decrease in tumor size. Additionally, biosafety and biochemical assessment performed in mice displayed no significant difference between NP treatment and control groups. Overall, our folic acid AgIONPs displayed excellent potential in the simultaneous application for safe and successful targeted synergistic photothermal treatment and imaging of a cancer model.

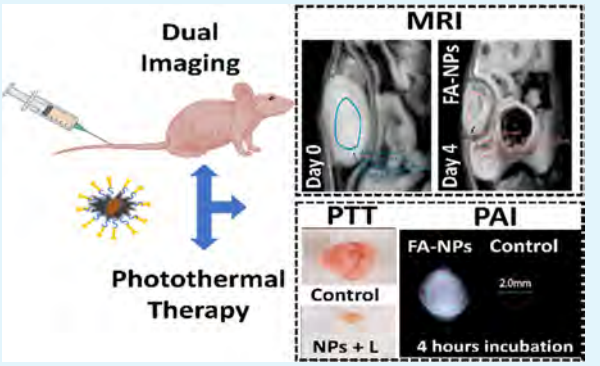

KEYWORDS: *nanoparticles, silver, iron oxide, cancer, photothermal, magnetic resonance imaging, photoacoustic imaging*

1. INTRODUCTION

Cancer is one of the leading causes of death globally, with 18.1 million new cases worldwide in 2018, and is anticipated to rise to over 24 million in 2030.[1] Generally, cancer therapies involve surgery, radiation, and chemotherapy. Conventional intravenous chemotherapy is not efficacious for the treatment of cancer due to the poor bioavailability, whereby the required therapeutic concentration is not attained as the drug does not reach the target tumor site.[2] Additionally, repetitive intravenous infusion of chemotherapy results in the development of drug resistance, which leads to poor efficacy and prognosis in patients.[3] Hence, nanotechnology provides a platform to deliver targeted therapies selectively to cancer cells, which is aimed at enhancing therapeutic efficacy and reducing adverse effects and multidrug resistance associated with conventional cancer treatment. Innovative strategies must be explored to develop effective treatment and diagnosis to improve a patient's prognosis. Nanophotothermal therapy (NPTT) based on the ability of nanoparticles (NPs), which converts near-infrared (NIR) light to generate heat, which selectively ablates tumor cells, has garnered immense interest as an alternative to or complementary strategy in the treatment of solid tumors. Notably, the acidic and hypoxic microenvironments of tumors are more susceptible to temperature rise in comparison to normal tissues.[4] Consequently, a temperature range between 40 and 45 °C can initiate a cascade of apoptotic events in tumors including protein denaturation, mitochondrial swelling, and rupture of the cell membrane.[4] Importantly, PTT confers unique advantages including its noninvasiveness, minimal damage to surrounding tissues, short recovery period, and temporal and spatial selectivity.[5] In the past few years, many researchers have demonstrated high efficacy of nanophotothermal therapy as an effective standalone treatment or synergistic therapy that is free of ionizing radiation damage.[6,7]

Silver nanoparticles (AgNPs) have been employed for various biomedical applications due to their inherent characteristics including antibacterial, antifungal, antiviral, anti-inflammatory, antiangiogenic, improving wound healing, and anticancer.[8] Recently, several groups have demonstrated the

Received: April 5, 2023
Accepted: August 8, 2023
Published: August 21, 2023

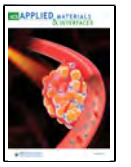

Scheme 1. : Schematic Illustration of the NP System that Consists of an Iron Oxide Core Coated with Silver, which Was Successfully Tuned to Near Infrared (NIR) and Decorated with Folic Acid (FA-PEG-SH) Ligands for Enhanced Targeting in U87MG Tumor for Synergistic Photothermal and Dual-Modal Imaging with Magnetic Resonance Imaging (MRI) In Vivo and Photoacoustic Imaging (PAI) In Vitro

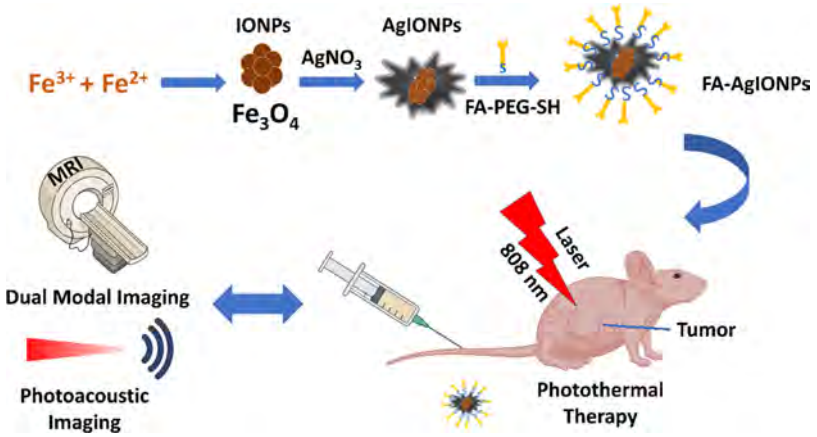

therapeutic efficacy of AgNPs based on their inherent characteristics that inhibit proliferation and induce apoptosis in cancer cells. Additionally, the unique surface plasmon resonance (SPR) properties of silver present it as a suitable agent for photothermal therapy, whereby conversion of absorbed photons of the laser into heat energy results in temperature elevation. Plasmonic metals like gold and silver display enhanced photostability and stronger light absorption abilities owing to their unique SPR in comparison to conventional photoabsorbing dyes.[9] Nonetheless, while silver exhibited the highest efficiency of SPR in the visible range, gold NPs have been intensively employed as photothermal agents for treatment in various cancer models. Owing to silver's high efficiency of SPR, Ag represents an appropriate potential alternative based on the enhanced photothermal conversion ability, which translates to enhanced efficacy accompanied by its cost-effectiveness in comparison to gold.[10] Contrastingly, to date, only one recent study has demonstrated the ability of Ag in an NP complex as a photothermal transducer in the treatment (465 nm laser, 0.95 W for 20 min) of a breast cancer model in vivo.[11] These NPs were functionalized with the human epidermal growth factor receptor 2 targeting ligand that is highly expressed in breast cancer cells.[12] While they displayed complete tumor regression, it should be highlighted that laser irradiation was performed at 465 nm, which was in the visible light spectrum and not in the NIR spectrum.[11] Consequently, it is highly crucial that laser exposure is performed at the NIR range as light is weakly absorbed by various components such as hemoglobin or melanin in tissues in comparison to visible light, thus allowing deep penetration of NIR light accompanied by minimal damage to healthy or surrounding tissues. Hence, NPs with strong absorbance in the NIR can be exploited as an anticancer therapeutic strategy via conversion of NIR light to generate heat, which results in localized temperature increment to selectively kill cancer cells and allow simultaneous photoacoustic imaging.[13,14] Also, the NP system developed for the above-mentioned study is specifically focused on photothermal therapy without the utilization of imaging modality.[11] Additionally, this study highlighted the targeting ability of its NP system, but it should be noted that in vivo administration was performed intratumorally, and no therapeutic comparison was performed with nontargeted groups to confirm the enhanced efficacy of targeting HER2 receptors.[11]

Magnetic resonance imaging (MRI) and photoacoustic imaging (PAI) are emerging as suitable and safe medical imaging techniques for this purpose due to their noninvasiveness, lack of ionizing radiation, high spatial resolution, and enhanced tissue penetration depth. These advantageous attributes allow real-time monitoring of NP accumulation and biodistribution in many preclinical studies.[15] While each imaging strategy has its advantages and drawbacks, combining the utilization of different imaging modalities for monitoring NP biodistribution and therapeutic efficacy can overcome limitations involved with an individual technique.[16]

Iron oxide-based NPs have been widely utilized as MRI contrast agents for the imaging of various disease models.[8,17−29] Areas where superparamagnetic iron oxide (SPIONPs) accumulate produce an intense negative contrast specifically in T_2/T_2* weighted MR images and appear hypointense or dark on images.[16] IONPs are predisposed to aggregation, and coating them with noble metals enhances their stability[30] while demonstrating a strong negative contrast for MRI and a strong absorbance in the NIR (680−850 nm). Hence, the development of multifunctional nanoplatforms composed of AgNPs and iron oxide nanoparticles (IONPs) can be carried out to exploit both MRI and PA imaging modalities.

Many researchers have functionalized NPs with targeting ligands to enhance NP accumulation in tumor sites, increase efficacy, and reduce adverse effects on normal tissues.[31,32] Among the various tumor-targeting receptors, folate receptor α (FRα) has gained intense interest due to its overexpression in 40% of the epithelial tumors including ovarian, kidney, uterine, colon, lung, and breast cancer accompanied by a restricted expression in normal tissues.[33,34] Consequently, several studies have reported an enhanced uptake of NPs targeting FRα and improved therapeutic efficacy in various cancer models.[35−37]

Recently, Kim et al. developed bovine serum albumin-coated AgNPs (spherical, 121 nm) and demonstrated their photothermal treatment application (690 nm laser, 1 W for 10 min) based on the effective inhibition of melanoma cell proliferation in vitro via induction of reactive oxygen species (ROS).[14] Nonetheless, this paper did not further study the efficacy of

https://doi.org/10.1021/acsami.3c04696
ACS Appl. Mater. Interfaces 2023, 15, 42153−42169

NPs as PTT agents in vivo or demonstrated their imaging ability.[14] While gold-based NPs have been extensively explored as PTT agents in the NIR in in vivo cancer models, silver NPs have yet to be exploited for this purpose. Hence, for the first time, we designed a novel silver−iron oxide nanohybrid, which was successfully tuned at the NIR to be effective in a targeted photothermal treatment strategy and dual-imaging ability using MRI (both in vitro and in vivo) and PAI (in vitro) in anticancer therapy (Scheme 1). The excellent anticancer activity of this NP system is conferred by the inherent anticancer properties of Ag and by photothermal temperature elevation upon laser irradiation at NIR. Additionally, these nanoparticles are decorated with ligands (FA-PEG-SH and mPEG-SH) targeting FRα that are overtly expressed in many cancers, notably in brain cancer (about 90% expression), to enhance the stability of NPs, the delivery, the accumulation, and the therapeutic efficacy in a murine glioma model.[38]

2. METHODS

2.1. Materials. All nonlisted chemicals were purchased from commercial suppliers at an analytical grade. Trisodium hydrate dihydrate (TSC), nitric acid, and isopropanol were purchased from Merck. Silver nitrate, iron, hydroxylamine 50%, sodium hydroxide, mPEG-SH (6000 g/mol), agarose low gelling, the Annexin-V FITC apoptosis detection kit, 2′,7′-dichlorofluorescin diacetate (DCFDA), and the Corning Matrigel Basement Membrane Matrix were purchased from Sigma-Aldrich. PrestoBlue was purchased from Invitrogen (Thermo Fisher Scientific). FA-PEG-SH was purchased from Ruixibiotech. Water used in all experiments was deionized water (DI).

2.2. Synthesis of IONPs. A 40 mL Fe^{2+}/Fe^{3+} solution including 2.66 g of $(NH_4)_2Fe(SO_4)_2{\cdot}6H_2O$ and 2.35 g of $FeCl_3{\cdot}6H_2O$ was made and added to a three-neck flask. Then, 2 mL of citric acid (25 mg/mL) was added. The reaction was kept under constant stirring and incubated at 95 °C for 30 min while the air was displaced from the reaction with nitrogen gas. Ammonia solution 30% (10 mL) was slowly injected into the mixture. The reaction was continuously maintained for 1 h at 95 °C under a nitrogen atmosphere. After that, the solution was centrifuged at 4350*g* for 6 min. The acquired pellet was washed repeatedly with citric acid buffer (pH 5.2) with the assistance of a high-intensity ultrasonic processor (Vibra-Cells, Sonics & Materials Inc.) until the IONPs were well-dispersed and did not precipitate under centrifugation (4350*g*, 6 min). The citrate-coated IONPs were dialyzed using a tube at MWCO 10 kDa for 48 h.

2.3. Silver Coating of Citrate-Coated IONPs. The final optimized protocol consisted of an aqueous solution of IONPs made with 0.144 mg of iron. 20 μL of 50% hydroxylamine and 70 μL of 1.14% trisodium citrate (TSC) solution were added into the solution under continuous stirring and served as a seeding agent for the elemental silver. 50 μL aliquots of $AgNO_3$ (6.348 mM) were added to the solution every 10 min until the amount of $AgNO_3$ added was 250 μL. Stirring at 500 rpm was carried out throughout the whole synthesis. An additional 75 μL of TSC (1.14%) was added at the end of the synthesis to stabilize the nanoparticles. The dense silver-coated iron oxide particles were separated from the less dense uncoated particles by centrifugation at 3500*g* for 7 min and redispersed in deionized (DI) water.[39] Dialysis was performed overnight with 5 L of water to purify the nanoparticles.

2.4. Characterization of NPs. Dynamic light scattering (DLS) (Litesizer, Anton-Paar) was employed to determine the size and ζ potential of the NPs. Transmission electron microscopy (TEM) images were taken on a JEOL-JEM-1010 TEM, operating at an accelerating voltage of 80 kV. We determined the absorption of the nanoparticles using a Clariostar UV−vis spectrophotometer for a wavelength range between 300 and 1000 nm. The concentrations of all of the metals were determined by inductively coupled plasma-optical emission spectroscopy (ICP-OES) (Optima 8300DV ICP-OES from PerkinElmer).

2.5. Conjugation of FA-PEG-SH and mPEG-SH to AgIONPs. The conjugation of FA-PEG-SH was conducted with a mass ratio of 1:25 of FA to NPs. After incubation for 1 h at room temperature with stirring at 450 rpm, mPEG-SH with a mass ratio of 1:1 of NPs to mPEG was added in the mixture. The reactions were carried out overnight at room temperature with stirring at 450 rpm. Samples were washed twice by centrifugation at 1000*g* for 6 min and redispersed in DI water. The ζ potential and the size of the particles were measured.

2.6. Stability of FA-PEG-AgIONPs in PBS (pH 7.4). To assess the stability of the coated nanoparticles, 100 μL of 10× PBS at pH 7.4 was added to 900 μL of NP solution in water. UV−visible spectra were recorded at different time points using a Clariostar UV−vis spectrophotometer in the range of 300−900 nm. Dynamic light scattering (DLS) was conducted to obtain hydrodynamic size and size distribution at the same time points.

2.7. Photothermal Ability of NPs. In a 96-well plate, photothermal effects of NPs in solution were evaluated based on the increment in temperature of different concentrations of NPs upon laser exposure at 808 nm under varying laser powers. Thermographic images and temperature were recorded using a thermal camera.

2.8. Phantom Magnetic Resonance Imaging (MRI) and Photoacoustic Imaging (PAI). The MRI scans and T_2 relaxation time of the AgIONPs at various concentrations were acquired using a Bruker 9.4 T MRI scanner running Paravision 6.0.1 at the Centre of Advanced Imaging (CAI), University of Queensland (St Lucia, Brisbane). T_2 values were calculated using a two-dimensional (2D) multislice multi-echo spin echo sequence using TR = 2630 ms, TE = 60 ms, 32 echoes, 0.117 mm × 0.117 mm in-plane resolution. The acquisition time was 11 min, 13 s. The T_2-weighted relaxivity (r_2) is defined as the slope of the linear regression plotted from the measured relaxation rate ($1/T_2$) versus the concentration of the contrast agent Fe.

All photoacoustic experiments were performed with a preclinical multispectral optoacoustic tomography (MSOT) inVision 256 (iThera Medical, Munich, Germany) with a 270° array of transducer detector elements and a central ultrasound frequency of 5 MHz. Laser radiation was generated from a Q switched Nd:YAG laser with a pulse duration of 8 ns and a repetition of 10 Hz. Photoacoustic data processing and quantification were performed using the ViewMSOT 3.8 software suite (iThera Medical) with images reconstructed using a back-projection algorithm. PA spectroscopy was acquired at 25 °C between 680 and 980 nm with a step size of 5 nm, using 3 averages per wavelength. PA spectroscopy measurements were obtained over a section of the phantom vessel with a step size of 0.5 mm. PA signal intensity was recorded as the mean pixel intensity of a region of interest (ROI) drawn within the internal diameter of the phantom, excluding the phantom vessel wall thickness. The PA spectrum was averaged over the scan range, and recorded spectra are displayed as the averaged signal over the phantom vessel scan range.

2.9. In Vitro Studies. *2.9.1. Cell Culture.* Cancer cells U-87 MG, HCT-116, B16-F10, SK-OV-3, and MDA MB-231 and nonmalignant cells such as CHO cells were attained from the American Type Culture Collection (ATCC). U-87 MG cells were maintained in DMEM low glucose (1 g/L), B16-F10 in DMEM high glucose (4.5 g/L), and the remaining cell lines in an RPMI 1640 medium at 37 °C in a humidified atmosphere with 5% CO_2. All growth media were supplemented with 10% fetal bovine serum (FBS), 100 U/mL penicillin, and 100 U/mL streptomycin. Cells were passaged or seeded for experiments at approximately 90% confluency.

2.9.2. In Vitro Cell Uptake of NPs. Cells were seeded in a six-well plate at a density of 500,000 cells/well and allowed to attach overnight. Cells were treated with NPs (with and without FA) at a concentration of 100 μg/mL for 4 and 24 h. Subsequently, cells were washed with DPBS 3 times, detached, and centrifuged at 200*g* for 5 min. The cell pellets were resuspended with 200 μL of warm 1% low-gelling-temperature agarose. 50 μL of cells in agarose was quickly transferred into a prepared phantom vessel and allowed to solidify at room temperature. T_2* values were determined using a 2D multigradient echo (MGE) sequence with TR = 300 ms, TE = 48 ms, 16 echoes, and 0.117 mm × 0.117 mm in-plane resolution. The

https://doi.org/10.1021/acsami.3c04696
ACS Appl. Mater. Interfaces 2023, 15, 42153−42169

acquisition time was 5 min 7 s. NP uptake was assessed by means of PA characterization, where the PA spectrum of the incubated cell phantoms was measured between 680 and 980 nm. The PA spectrum was averaged over five phantom vessel positions in a sequential methodology. The PA signal intensity was recorded as the mean pixel intensity of a region of interest (ROI) drawn within the internal diameter of the phantom, excluding the phantom vessel wall thickness.

2.9.3. Cytotoxicity Assay. Cells were seeded into 96-well plates at cell densities of 10,000 cells/well and allowed to attach overnight. Cells were treated with different concentrations of NPs for 24 h. For laser groups, media was replaced with fresh media and cells were irradiated with an 808 nm infrared laser (light intensity= 1.5 W/cm^2, laser diameter= 2 cm) for 5 min in a custom-build stabilized infrared fiber laser system (MDL-II-808 laser, EFORCE AUSTRALIA PTY LTD.). Temperature was recorded using a thermal camera (FLIR CX-Series). After treatment, cells were incubated with a 1× PrestoBlue cell viability reagent for 30 min at 37 °C and 5% CO_2. Viable cells were detected by fluorescence intensity measurement using a CLARIOstar *Plus* plate reader (BMG Labtech) at 560/590 nm (excitation/emission). The fluorescence of nontreated cells was determined as 100% cell viability.

2.9.4. Intracellular ROS Assay. U-87 MG cells were seeded in 96-well plates at a density of 10,000 cells/well and allowed to attach overnight. To determine the ROS regulating effects of NPs, cells were first treated with different concentrations of AgIONPs in growth media for 24 h, washed with DPBS, and stained with a 25 μM DCFDA reagent in supplemented DPBS (10% FBS in DPBS) for 45 min at 37 °C and 5% CO_2. Intracellular ROS levels were measured by taking fluorescence readings at 485/535 nm (excitation/emission) using a CLARIOstar *Plus* plate reader (BMG Labtech). The fluorescence intensities of treated wells were normalized against nontreated wells to determine the fold change of the intracellular ROS level.

2.9.5. Cell Apoptosis Assay. The Annexin-V-FITC assay was utilized to assess the apoptosis of U87MG cells (1×10^5 cells/well) in 24-well plates. After 24 h, cells were treated with 100 μg/mL NPs for 24 h. For the laser group, cells were further exposed to the laser at 1.5 W/cm^2 for 5 min. For flow analysis, all attached and floating cells were collected and washed thrice with PBS. Cells were suspended in binding buffer and stained with Annexin-V-FITC and propidium iodide (PI) for 15 min in the dark. Stained cells were analyzed using the Accuri6 cytometer and Flowjo software.

2.10. In Vivo Study. *2.10.1. Animal Study.* Animal studies were conducted at the Centre of Advanced Imaging (CAI), University of Queensland (St. Lucia, Brisbane), in accordance with the national guidelines provided and approved by the institutional animal care and ethics committees of the University of Queensland (# 2021/AE001086). All animals were sourced from Animal Resources Centre (Murdoch, Perth) and acclimatized for a full 7 days at a CAI animal holding room prior to commencement of experiments. Procedures including tumor induction, treatment administration, MSOT and MR imaging, and terminal blood collection were performed on mice placed under isoflurane anesthesia (1−4% isoflurane with an air−oxygen mixture at a flow rate of 0.4−1 L/min). Throughout the experimental period, animals were monitored for signs of distress or ill health with appropriate husbandry and supportive therapies including deep and clean supportive bedding, a warm, quiet, and dim environment, fluids, and food and water in a palatable readily available form provided.

2.10.2. Biosafety Assessment. 10-week-old female C57BL/6J mice were randomly divided into three groups and administered with saline (n = 4), (5 mg/kg Ag, n = 4) (10 mg/kg Ag, n = 4) via intravenous (IV) tail vein injection on days 0, 4, and 8 to assess the biocompatibility of NPs. Mice were monitored every 2 days for changes in their body weight. On day 12, mice were placed under deep anesthesia, and 600−800 μL of blood was collected from each mouse by cardiac puncture. The whole blood was left undisturbed at room temperature for 30 min to allow clotting and then centrifuged at 4000g for 30 min at 4 °C. The resulting supernatant (serum) was collected immediately and stored at −20 °C for further biochemical analysis. Clinical chemistry analysis of serum (glucose, bilirubin, albumin, alanine transaminase, creatinine, urea, and uric acid) was completed on a Beckman Coulter AU480 analyzer (Lane Cove, Australia). Frozen aliquots were thawed and centrifuged at 21,500g for 10 min (room temperature) prior to analysis. All analyses were conducted after the instrument passed calibration (system check) and quality control. Samples were analyzed in single or duplicate, with duplicate measures averaged. Data were compared to reference ranges for rodents (rats) as per published results.[40] After blood collection, major organs including the heart, lung, liver, spleen, and kidney were harvested for weighing and then stored in 4% PFA solution, sliced, and stained with hematoxylin and eosin (H&E) for histological analysis.

2.10.3. Therapeutic Efficacy. To establish tumor models, 10-week-old mixed-gender BALB/c nude mice were each subcutaneously injected with 100 μL of U-87 MG cells (7.5×10^6 cells suspended in a 1:1 ratio of a Matrigel Basement Membrane Matrix and an L-15 medium) into the right flank. The tumor size was monitored every other day using a digital vernier caliper, and the tumor volume (V) was calculated using the following formula: $V = (\text{length} \times \text{width}^2)/2$. When the tumor volume reached 100−150 mm^3, mice were randomly divided into four groups (n = 5) and intravenously injected through the tail vein with 100 μL of saline, AgIONPs (10 mg/kg), FA-AgIONPs (10 mg/kg), and FA-AgIONPs (10 mg/kg) + laser irradiation. The anticancer efficacies of the treatment groups were assessed by monitoring the tumor volume and body weight every 2 days. At the end of the experiment, mice were sacrificed, and tumors were weighed and harvested. TUNEL assay of tumors was performed using a kit (ab206386) as per the manufacturer's instructions.

2.10.4. Targeting Efficacy. 2.10.4.1. Magnetic Resonance Imaging (MRI) Efficacy. Anesthetized mice were placed in a 300 mm bore 7 T ClinScan preclinical MR Scanner running Siemens VB17 (Bruker/Siemens). A mouse body radiofrequency coil with an inner diameter of 40 mm was used to acquire MR images at 0, 1, and 4 days post the first IV injection (FA-AgIONPs and AgIONPs). The following images were acquired with the relaxation time determined from the T_2 and T_2* images automatically calculated by the operating system.

1. Localizer images: Three orthogonal gradient echo images were acquired with the following parameters: TR = 23 ms, TE = 4.43 ms, field of view 100 mm × 100 mm, slice thickness = 1 mm, matrix = 256 × 256, flip angle = 25°, pixel bandwidth = 260 Hz/Px, and total scan time = 18 s.
2. 2D T_2 spin echo images: 2D spin echo images were acquired using the following parameters: TR = 1200 ms, TE = 12.7 ms, field of view 30 mm × 30 mm, slice thickness = 1 mm, number of slices = 130, slice gap = 1.2 mm, image matrix = 192 × 192, flip angle = 180°, pixel bandwidth = 130 Hz/Px, and total scan time = 30 min/mouse.
3. 2D T_2* gradient echo images—2D gradient echo images were acquired using the following parameters: TR = 1600 ms, TE = 4 ms, field of view 39 mm × 39 mm, slice thickness = 1 mm, number of slices = 32, slice gap = 1.2 mm, image matrix = 192 × 192, flip angle = 20°, pixel bandwidth = 704 Hz/Px, total scan time = 30 min/mouse.

2.10.4.2. MSOT Photoacoustic Imaging Efficacy. MSOT imaging was performed immediately after MRI. Anesthetized mice were positioned in a supine position within the animal holding frame with 2% isoflurane and an O_2 flow rate of 0.4 L/min, coated with ultrasound coupling gel, and wrapped in a thin polyethylene membrane. Air pockets were absent within the vicinity of the tumor volume. Mice were submerged within the 37 °C imaging chamber and positioned within the 270° ultrasound transducer array with the scan range defined to correspond with the tumor position. Mice were z-translated through the imaging plane in 0.3 mm steps to acquire a stack of 2D axial images over the scan region. Ten frames per wavelength at 680, 700, 730, 760, 800, 850, and 900 nm were acquired. Images were reconstructed with a back-projection algorithm

https://doi.org/10.1021/acsami.3c04696
ACS Appl. Mater. Interfaces 2023, 15, 42153−42169

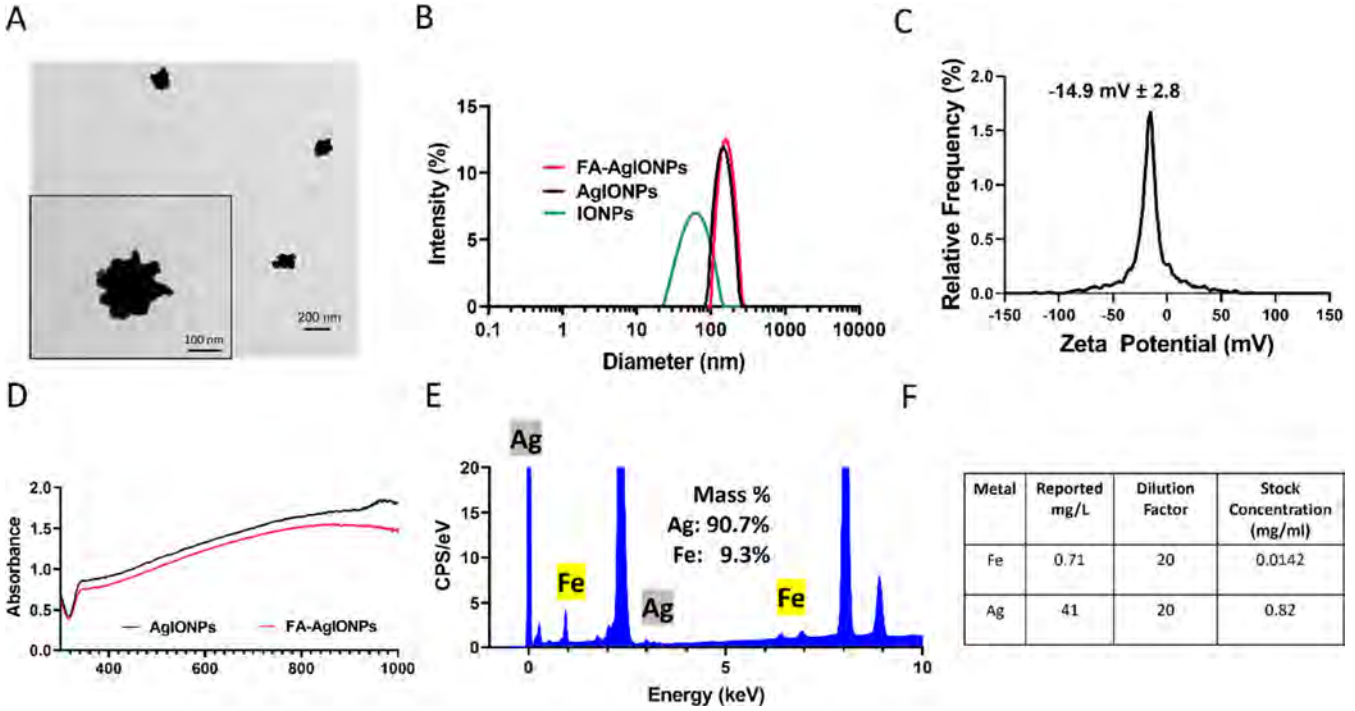

Metal	Reported mg/L	Dilution Factor	Stock Concentration (mg/ml)
Fe	0.71	20	0.0142
Ag	41	20	0.82

Figure 1. Characterization of AgIONPs. (A) TEM images showing AgIONPs with an irregular nanorose-like shape. (B) DLS of the nanoparticles demonstrating the size intensity (%) distribution of AgIONPs. (C) ζ potential peak of FA-AgIONPs. (D) Absorbance of NPs showing an intense peak at 808 nm NIR. (E) Energy-dispersive spectroscopy (EDS) spectrum depicts the percentage of both metals in AgIONPs. (F) ICP Fe and Ag analysis of the synthesized NPs.

and processed using a linear spectral-unmixing algorithm to identify the signal of oxyhemoglobin (HbO_2), hemoglobin (Hb), and the AgIONPs. A fluence correction algorithm was applied to the MSOT images post reconstruction. An ROI was defined in the *XY* plane of a single image frame set at the center of the tumor volume for quantitative analysis.

2.11. Statistical Analysis. Data are presented as the mean ± standard deviation. One-way ANOVA and Student's *t* test were employed for significance testing with a *p* value ≤0.05 considered statistically significant. Data analyses were performed using GraphPad Prism (GraphPad Software Inc.)

3. RESULTS AND DISCUSSION

3.1. Synthesis and Characterization of IONPs, AgIONPs, and FA-PEG-AgIONPs. IONPs were successfully synthesized with the coprecipitation of Fe(II) and Fe(III) chlorides in an alkaline solution at a high temperature. The hydrodynamic size of IONPs was 58.3 nm (Figure 1B) with a homogeneous distribution with a polydispersity index (PDI) of 0.188 (Table S1). These IONPs were stable and displayed no aggregation. The TEM image corroborates DLS data, displaying a uniform size and IONPs appearing as clusters (Figure S1A,B). The IONPs had a negative surface charge with a ζ potential of −45.8 mV (Figure S1C) due to the citrate coating. The main purpose of the iron oxide core is for the utilization of MRI, whereby an accumulation of NPs results in a generation of negative contrast, particularly in T_2/T_2^* weighted MR images, and it appears hypointense or dark on images.[19] The iron oxide core will not affect the efficacy of Ag coating outside as IONPs are predisposed to aggregation and coating them with Ag improves its stability[30] while demonstrating a strong negative contrast for MRI and a strong absorbance in the NIR (680−850 nm), hence allowing a multifaceted NP system, whereby both MRI and PAI images can be acquired.

The iron oxide core also functioned as a surface template for the silver ion coating and acted as a donor of electrons for the growth of the Ag layer. The silver coating was formed via a seeding technique, whereby reducing agents were employed to reduce the salts in the silver nitrate solution.[39] Here, the seedings of silver nucleation were developed by the utilization of sodium citrate, hydroxylamine, and the citrate-coated iron oxide nanoparticles. Subsequently, the addition of silver nitrate aliquots formed a silver seed on the surface of the IONPs. Previously reported studies from our group have demonstrated that the mass ratio between silver and iron (Ag/Fe) and the amount of hydroxylamine employed are crucial for the asymmetrical spiky shaped NPs and their strong absorbance in the NIR.[8,39] The optimized protocol involves the utilization of 20 μL of 50% hydroxylamine and a 1.18 mass ratio of Ag/Fe in the reaction. It should be noted that preliminary imaging studies of NPs were performed to ascertain both MRI and PAI contrast abilities to confirm parameters such as the Ag/Fe ratios in the synthesis reaction as these NPs were developed to be effective in both photothermal treatment strategy and dual-imaging ability using MRI and PAI. The iron oxide core was coated with silver nitrate on the surface also possibly via electrostatic interactions between the electrons from the silver and surface of the oxide. Here, the coating of silver on the surface of IONPs is achievable based on the highly negative charges of the citrate-coated IONPs. Indeed, without the iron oxide core, spiky AgIONPs could not be formed.

The seedings of silver nucleation are formed when silver is reduced by citrate and hydroxylamine, which resulted in asymmetrical spiky shaped NPs due to the presence of small clusters of silver NPs formed stemming from the high negative

https://doi.org/10.1021/acsami.3c04696
ACS Appl. Mater. Interfaces 2023, 15, 42153−42169

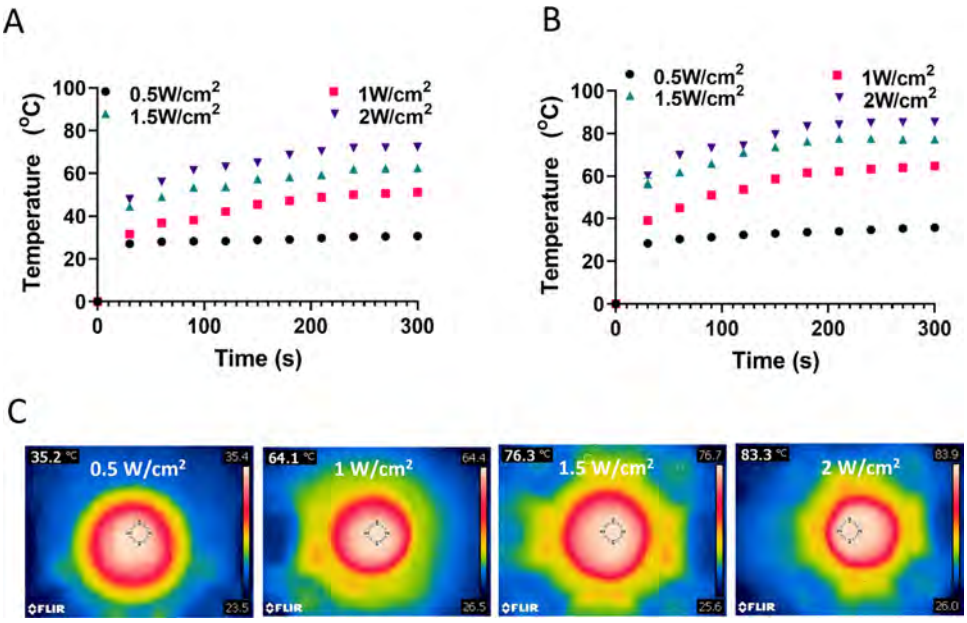

Figure 2. Photothermal temperature elevation of FA-conjugated AgIONPs under laser exposure. The solutions with different concentrations of NPs were irradiated with an NIR laser for 5 min at different power densities of 0.5−2 W/cm^2: (A) 50 μg/mL and (B) 100 μg/mL. (C) Corresponding representative NIR thermographic images of the wells containing NPs (100 μg/mL) at the 300th second.

surface electric charge of IONPs.[41] More nucleation will occur as more silver is added on the surface of the existing layer resulting in the spiky asymmetrical morphology of NPs and hence an enhanced plasmon resonance and strong absorbance in the NIR.[41] TEM images (Figure 1A) confirmed a uniform size and asymmetrical spiky shaped NPs due to the deposition of a high mass of silver, which contributes to a high plasmon resonance and high absorption in the NIR.[41,42] Additionally, NPs with lower symmetry demonstrated the lower energy and higher efficiency of SPR, which are capable of enhanced PTT efficacy in the NIR in comparison to its more symmetric counterparts.[43] The resulting AgIONPs demonstrated an average hydrodynamic size of 165.3 nm with a low PDI of 0.06 and were negatively charged at −28 mV (Figure 1B and Table S1). Naïve AgIONPs without pegylation, whereby size and UV−vis absorbance were significantly impacted upon addition of PBS, were not stable and aggregated in a short period of time. Bare NPs can be quickly identified and cleared from circulation in vivo via the reticuloendothelial system, which majorly limits their migratory ability to the tumor.[44] Pegylation for enhanced stability and folate targeting can be effectively exploited by NPs in anticancer application with previously reported studies demonstrating enhanced uptake and efficacy in comparison to untargeted NPs as FA attaches firmly to FRα in cancer cells and are internalized via endocytosis, after which FRα are recycled back to the cell surface.[38] Here, AgIONPs were decorated with different concentrations of FA-PEG-SH targeting FRα that are highly expressed in many cancers specifically in brain cancer to enhance the stability of AgIONPs, delivery, accumulation, and therapeutic efficacy in the U87MG murine model. mPEG-SH was added to confer enhanced stability of NPs. Based on the stability of NPs in PBS (Tables S2 and S3), size, and PDI, mass ratios of 1:25 of FA/NPs and 1:1 of NPs/mPEG were selected as the optimized parameters (Table S4). Upon conjugation of FA-PEG-SH and mPEG-SH, the size of the NPs increased to 175.6 nm, the ζ potential became less negative at −13.4 mV (Figure 1B,C), and the PDI was much lower at 0.006, demonstrating successful conjugation of the FA targeting ligand and enhanced uniformity of NPs (Figure 1B,C). Previous studies had displayed that the slightly negatively charged NPs demonstrated enhanced accumulation in tumors; hence, these targeted NPs presented themselves as favorable for homing toward tumor sites.[45,46] Additionally, FA-AgIONPs demonstrated an improved stability of 74% after a period of 1 week in PBS, displaying an average hydrodynamic size of 171.2 nm and a PDI of 0.19 without noticeable aggregation (Table S3). Importantly, UV−vis spectra (Figure 1D) illustrated a clear maximum absorbance peak in the NIR range, suggesting successful tuning of the SPR effect of AgIONPs to the desirable NIR range for biomedical applications. Additionally, no significant difference was observed in the shape of the spectra between AgIONPs and FA-AgIONPs, suggesting that the good stability of the NPs resulted from the successful conjugation of FA-PEG-SH and mPEG-SH to the NPs. EDS (Figure 1E) showed the presence of both Fe and Ag with mass % of 9.3 and 90.7%, respectively, and ICP data (Figure 1F) demonstrated a smaller presence of Fe at 1.7% and Ag at 98.3%, in the AgIONP sample. This displayed difference could be due to the limitation of EDS, whereby 1 NP is analyzed in comparison to ICP, which analyzes a group of NPs to obtain the concentrations of Ag and Fe. Additionally, the asymmetric spiky morphology of the NPs could have impeded the penetration of X-rays into the core of the NPs, hence impacting the accuracy achieved for EDS analysis.[47] Nonetheless, note that all in vivo studies are based on acquired ICP data.

3.2. Photothermal Effects of FA-AgIONPs. The photothermal effect of FA-AgIONPs was assessed by measuring the temperature elevation of different concentrations of NPs at different powers of NIR laser irradiation at 808 nm (0.5−2 W/cm^2) for up to 5 min. A thermal camera was utilized to record the temperature and obtain thermographic images. At 50 μg/mL FA-AgIONPs, the temperature increased to 31 °C at 0.5

https://doi.org/10.1021/acsami.3c04696
ACS Appl. Mater. Interfaces 2023, 15, 42153−42169

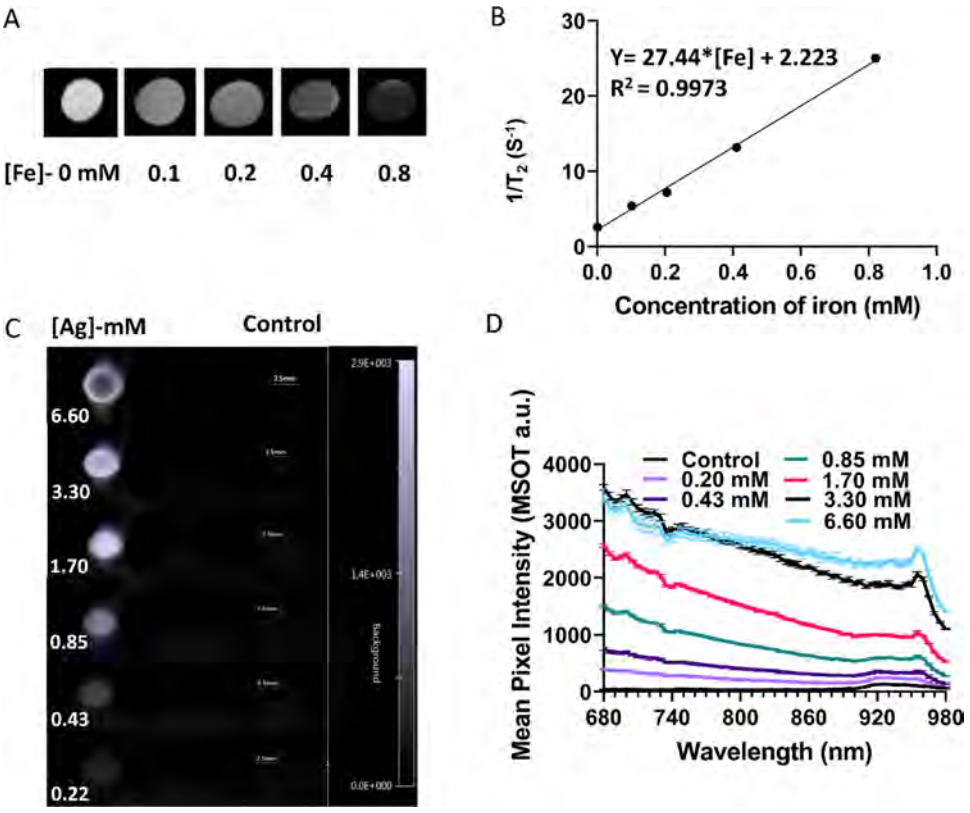

Figure 3. MRI and MSOT of AgIONPs. (A) T_2-weighted images of phantom tubes with AgIONPs showing an enhancement in the contrast signal with each increasing Fe concentration and (B) analysis of transverse relaxivity (r_2 = 27.44 mM^{-1} s^{-1}). (C) MSOT images of phantom tubes with AgIONPs showing an enhancement in the signal with each increasing concentration of Ag. (D) Photoacoustic spectrum of AgIONP phantoms showing an increase in signal intensity with increasing Ag concentration. Water is used as the control.

W/cm^2 and to an extreme high of 72 °C after 5 min (Figure 2A). At double the concentration (100 μg/mL), the temperature increased to 36 °C at 0.5 W and to an extreme high of 85 °C after 5 min (Figure 2B). Contrastingly, the temperature increase of PBS was negligible. Hence, these results demonstrated that the NIR-heating effect of NPs was dependent on the power, NP concentration, and length of time of laser exposure. Importantly, these NPs could rapidly and efficiently convert the absorbed photon into heat and act as photothermal agents for tumor ablation. The representative thermographic images at the 300th s are shown in Figure 2C. Additionally, the photothermal conversion efficiency was calculated to be 21.4% (Figure S2). A high photothermal conversion efficiency is an important aspect to ascertain the potential application of NPs in laser-induced photothermal therapy. Hence, the photothermal conversion efficiency attained here is within the desirable range based on previously reported studies on the successful application of gold NPs in anticancer PTT (conversion efficiency: 9−30.48%).[48−50]

3.3. MR and PA Contrast Efficacy. These NPs were developed to be effective in photothermal treatment strategy and dual-imaging ability using MRI and PAI. Hence, to evaluate the feasibility of NPs as dual-imaging contrast agents, first, different concentrations of FA-AgIONPs were prepared as MRI phantoms for assessment of the MR imaging ability (Figure 3A,B). The T_2-weighted images of phantom tubes with NPs demonstrated an enhancement in the contrast signal (darker images) with increasing Fe concentration (Figure 3A). This is due to the iron oxide core being a negative contrast agent, which shortens the transverse relaxation time T_2 of the surrounding protons. The transverse relaxivity (r_2), defined as the slope from the linear regression, which is a vital attribute in establishing the MRI efficacy of contrast agents, was analyzed to be 27.44 mM^{-1} s^{-1} at 9.4 T MR systems (Figure 3B). The T_2 contrast generated was adequately strong to acquire negative contrast enhancement on the MR images in vivo. Similarly, the photoacoustic efficacy was assessed over a series of NP concentrations to determine the PA response (Figure 3C,D). Correspondingly, the PA intensity increased with an increasing concentration of Ag. Figure 3C displays the PA phantom images, demonstrating enhancement in the PA signal (hyperintense signal) with an increasing concentration of Ag. However, at the highest concentrations of 6.6 and 3.3 mM Ag, the mean pixel intensity between these two concentrations was not distinctly different at 808 nm wavelength (Figure 3D). Hence, PAI results suggest that the signal achieved is dose-dependent. However, once the concentration of silver reaches 3.3 mM, a threshold is attained, and any further increase in Ag did not result in a further enhanced contrast signal due to reaching the upper limit of the optical density for these NPs in this equipment (Figure 3C,D).

The NP PA spectrum presents the highest PA signal at 680 nm and bathochromically tails to approximately 950 nm in a similar fashion to hemoglobin (Hb) (Figure 3D).[51] The observed peaks between 920 and 960 nm are artifacts of the solvent and phantom vessel as indicated by the PA spectrum of the solvent control. Interestingly, the AgIONP's PA spectrum does not correlate with the AgIONP's absorbance spectrum (Figure 1D), similar to observations made for organic PA dyes.[52] However, the AgIONP's PA spectrum (Figure 3D)

https://doi.org/10.1021/acsami.3c04696
ACS Appl. Mater. Interfaces 2023, 15, 42153−42169

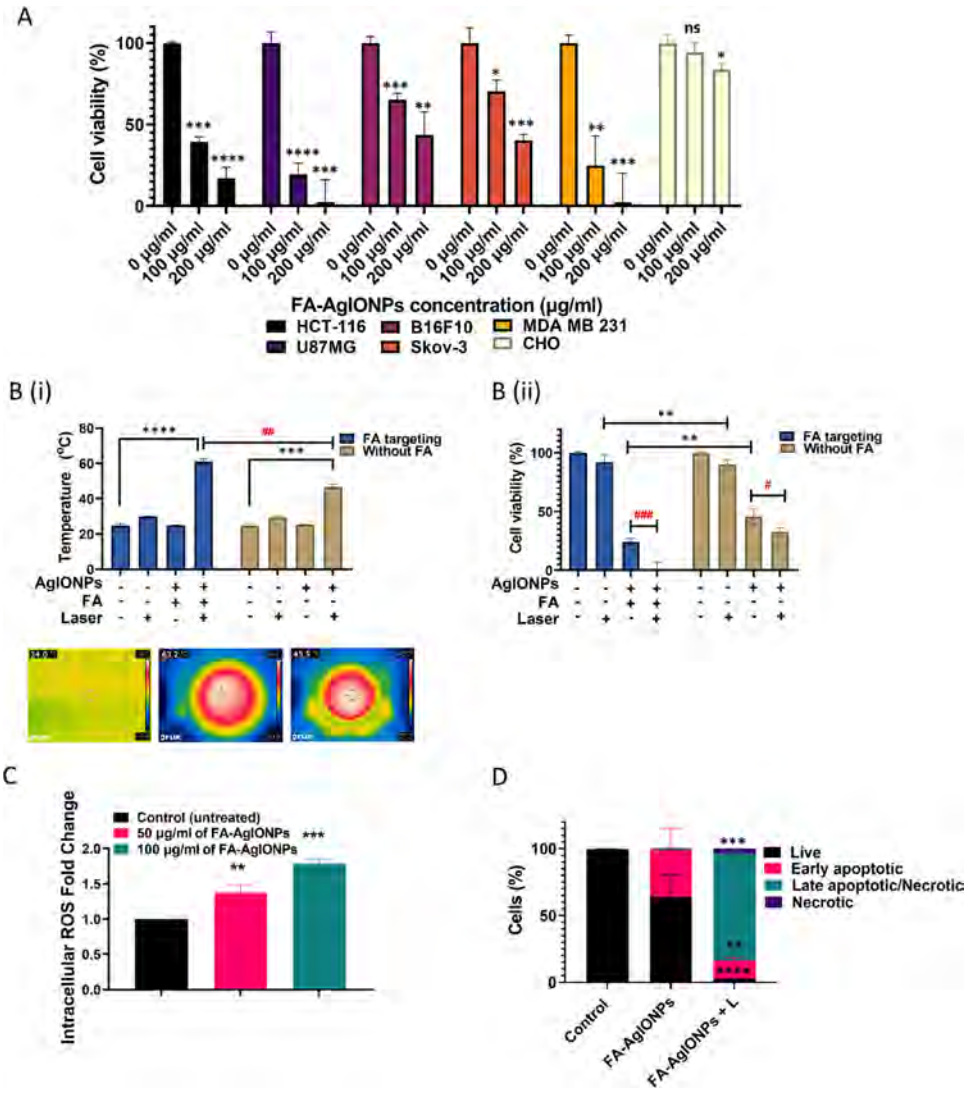

Figure 4. Cytotoxicity of cells incubated with AgIONPs with and without FA targeting. (A) A panel of cancer cell lines was treated with AgIONPs with the FA ligand at varying NP concentrations. * Compared to the respective control group (untreated cells): *$p < 0.05$, **$p < 0.01$, ***$p < 0.001$, ****$p < 0.0001$. (B(i)) U87MG cells treated with 100 μg/mL AgIONPs with and without FA targeting and exposed to laser irradiation at 1.5 W/cm^2, 5 min. Photothermal temperature elevation and corresponding representative NIR thermographic images of wells at the 300th second. * Compared with the control (no NPs and no laser). ***$p < 0.001$, ****$p < 0.0001$. # Compared with the addition of FA targeting. $^{\#\#}p < 0.01$ (B(ii)) Photothermal cytotoxicity in U87MG cells with and without laser. * Compared to respective groups with and without FA targeting. **$p < 0.01$. # Compared to the addition of laser exposure. $^{\#}p < 0.05$, $^{\#\#}p < 0.01$, (C) Intracellular ROS fold change of U87MG cells treated with 50 and 100 μg/mL FA-AgIONPs. * Compared to the control group (untreated cells). **$p < 0.01$, ***$p < 0.001$. (D) Flow cytometry analysis of U87MG cells treated with 100 μg/mL FA-AgIONPs to determine stages of apoptosis, laser (L) irradiation at 1.5 W/cm^2, 5 min. * Compared to the respective stages of the apoptosis cell population of the control group: **$p < 0.01$, ***$p < 0.001$, ****$p < 0.0001$.

does appear to correlate with the absorbance spectrum recorded for Ag-nanodots previously assessed for PAI.[53] Therefore, while the observed AgIONP absorbance spectrum is likely a consequence of the combined Ag−Fe localized SPR, the PA spectrum may not be associated with the NIR SPR band.[54] Consequently, the AgIONP's PA spectrum is likely solely associated with the nonradiative excited-state relaxation processes and kinetics of the Ag. However, these phantom results concluded that FA-AgIONPs can be utilized as reliable contrast agents for both MRI and PAI.

3.4. Cytotoxicity of AgIONPs and Photothermal Ablation in Cancer Cells. A panel of cancer cell lines (HCT-116, U87MG, B16-F10, Skov-3, and MDA MB-231) and CHO cells were treated with FA-AgIONPs for 24 h to assess the cytotoxicity of NPs in the proliferation of various cell lines using the PrestoBlue assay. Evidently, FA-conjugated NPs were significantly more toxic in all cancer cell lines in comparison to CHO cells (Figure 4A). Even at a high concentration of 200 μg/mL, the cell viability of CHO cells was 83.5% in comparison to U87MG cells at 2.5%, MDA MB 231 at 2.2%, HCT-116 at 17.1%, and B16-F10 at 43.6%, which demonstrated enhanced selectivity and cytotoxicity of targeted NPs in cancer cell lines. The heightened cytotoxicity of targeted NPs in cancer cell lines is due to the increased expression of FRα in these cancer cell lines in comparison to nonmalignant cells like CHO, which has been established as a non-FRα cell line.[55−57] Importantly, these NPs demonstrated good biocompatibility as they are not toxic in nonmalignant CHO cells, suggesting high suitability for biomedical applications. These results suggested that the conjugation of

https://doi.org/10.1021/acsami.3c04696
ACS Appl. Mater. Interfaces 2023, 15, 42153−42169

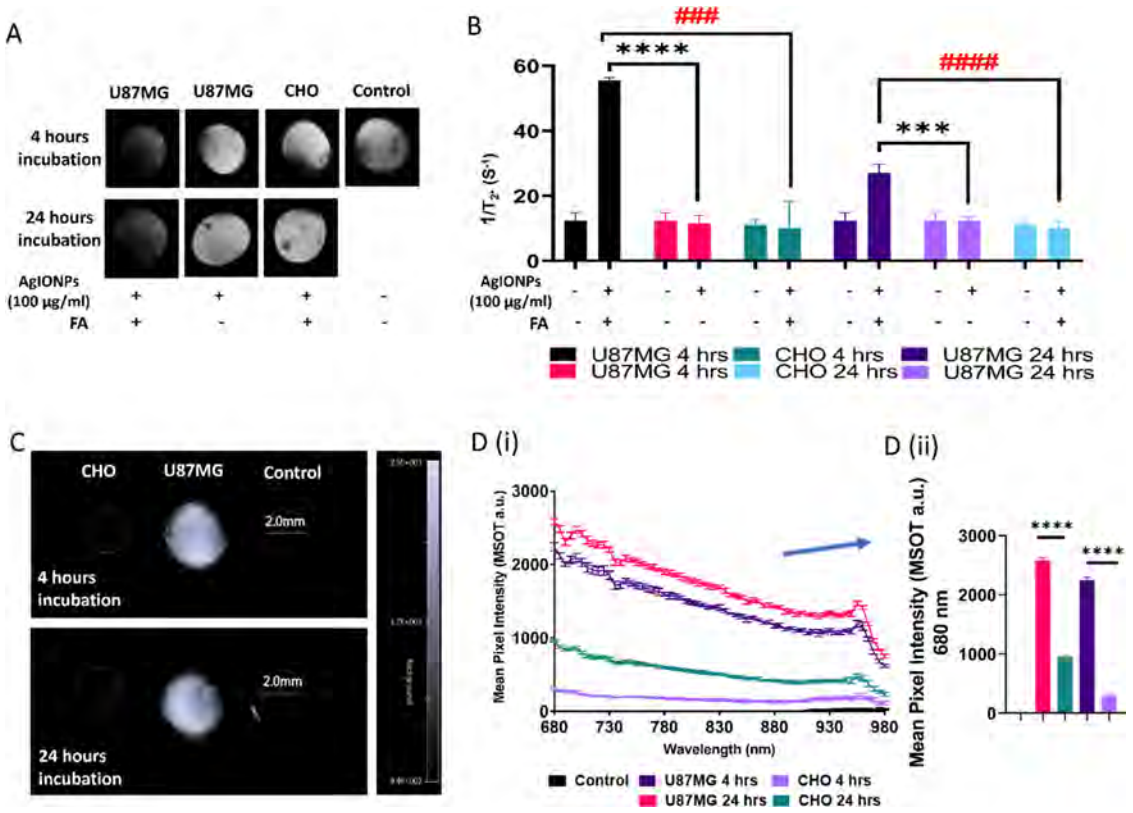

Figure 5. MRI and MSOT of cells labeled with AgIONPs with and without FA targeting. (A) T_2*-weighted images of cells labeled with AgIONPs in phantom tubes showing an enhancement in the contrast signal. (B) $1/T_2$* (s^{-1}) of U87MG and CHO cells incubated with 100 μg/mL AgIONPs with and without FA at 4 and 24 h. * In comparison with no FA. # In comparison with CHO at respective incubation time points. *** and $^{###}p < 0.001$, **** and $^{####}p < 0.0001$. (C) PA phantom images of U87MG and CHO cells labeled with 100 μg/mL FA-AgIONPs. (D) (i) Measured PA spectrum of incubated cell phantoms showing the PA intensity difference of the AgIONP spectra between U87MG and CHO cells. (ii) Mean pixel intensity at 680 nm of PA cell phantoms of U87MG and CHO cells labeled with 100 μg/mL FA-AgIONPs. * In comparison with CHO at respective incubation time points. $^{****}p < 0.0001$.

the FA ligand onto the AgIONPs could potentially minimize the adverse effects in healthy cells but be selectively cytotoxic to cancer cells. A lower concentration (100 μg/mL) of NPs resulted in a more significant cytotoxic killing of U87MG cells at a cell viability of 19.4% (* compared to respective untreated cells: $^{****}p < 0.0001$) in comparison to MDA MB 231 at 24.9% (* compared to respective untreated cells: $^{**}p < 0.01$. Figure 4A). Also, at double the concentration of NPs (200 μg/mL), the cell viabilities of U87MG and MDA MB 231 were 2.5 and 2.2%, respectively (*compared to the respective untreated cells: $^{**}p < 0.01$; similar statistical significance). Hence, based on the enhanced cytotoxicity of NPs at 100 μg/mL and the similar cell viability of both cell lines at 200 μg/mL NPs, the U87MG cell line was selected for further analysis.

For photothermal temperature elevation and cytotoxicity studies in vitro, U87MG cells were treated with 100 μg/mL AgIONPs with and without FA targeting for 24 h. Subsequently, treated cells were washed with PBS and exposed to laser irradiation at 1.5 W/cm^2 for 5 min. Cell viability was assessed before and after laser exposure. Results demonstrated cell viabilities of 24.4 and 45.7% in FA-NPs and nontargeted NP-treated groups, respectively, before laser exposure, indicating that the addition of the FA ligand amplified the cytotoxicity of AgIONPs most likely due to the enhanced uptake of targeted NPs in U87MG cells. Also, upon laser irradiation at 1.5 W/cm^2 for 5 min, the temperature increased to 60 °C with FA and to 48 °C without FA targeting (Figure 4B(i)). The temperature thresholds that were reached in both targeted and nontargeted NPs were still within the desired range between 43 and 60 °C required for induction of apoptosis in cancer cells.[58] The temperature increment with FA-targeted NPs was 12 °C higher than the nontargeted group, suggesting better uptake of targeted NPs, which led to a higher temperature elevation. Consequently, exposure to laser irradiation resulted in cell viabilities of 0 and 32.9% in targeted and nontargeted groups (Figure 4B(ii)), which corroborated the fact that FA conjugation enhances cytotoxicity of AgIONPs and photothermal laser resulted in further significant synergistic killing and total eradication of U87MG cells in vitro.

Typically, cancer cells display higher basal ROS levels in comparison to normal cells to sustain tumor development while maintaining ROS levels below the cytotoxic threshold. Hence, increasing the ROS levels by either reducing ROS scavenging or elevating ROS production above the cytotoxic threshold can generate oxidative stress, which leads to the induction of apoptosis in cancer cells, which already has higher-than-normal ROS levels.[32] Consequently, normal cells, which have intrinsically lower basal ROS levels, are not as sensitive to enhanced ROS production in comparison to cancer cells.[59] Here, intracellular ROS fold change was measured in U87MG cells treated with 50 and 100 μg/mL NPs resulting in 1.4- and 1.8-fold increases of ROS levels, respectively (Figure 4C). Moreover, the PI-Annexin-V FITC

https://doi.org/10.1021/acsami.3c04696
ACS Appl. Mater. Interfaces 2023, 15, 42153−42169

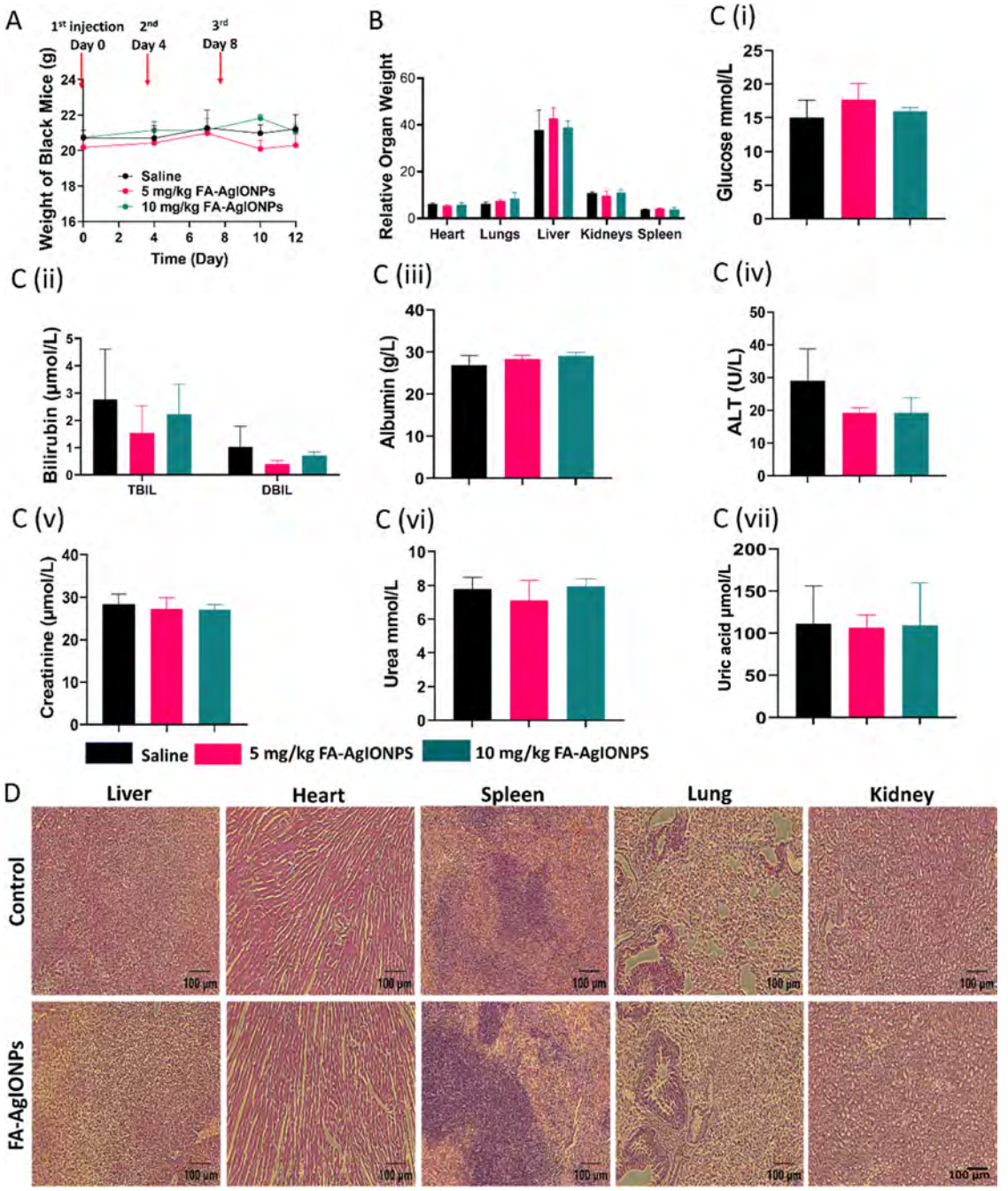

Figure 6. Biosafety studies of NPs in female C57BL/6J mice. Mice were injected intravenously with saline (control group) as well as with 5 and 10 mg/kg AgIONPs on days 0, 4, and 8 to determine the in vivo biocompatibility of the nanoparticles. (A) Average body weight of mice was monitored twice a week across the experimental period. (B) Organs including heart, lungs, liver, kidneys, and spleen were collected and weighed on day 12. Relative organ weights (organ-weight-to-body-weight ratios) were determined as mg organ weight/g terminal body weight of mice. (C) Biochemical analysis of serum from C57BL/6J mice. Blood samples were collected on day 12 via cardiac puncture. Purified serum samples from whole blood collected were tested for (i) glucose, (ii) bilirubin, (iii) albumin, (iv) alanine transaminase (ALT), (v) creatinine, (vi) urea, and (vii) uric acid. (D) Histological images of tissues stained with H&E indicating the status of major organs after animals were sacrificed on day 12 post i.v. injection.

kit was utilized to quantify the apoptotic and necrotic populations of U87MG cells treated with NPs only and the synergistic inclusion of laser exposure. In the control group, viable cells were at 99.6% and apoptotic and necrotic cells were negligible. In the NP-treated group, viable cell populations decreased to 63.9%, early apoptotic cells were at 35%, and late apoptotic and necrotic cells are negligible (Figures 4D and S3). However, upon laser exposure, the synergistic group displayed a statistically significant reduction in the viable cell population at 2.63% and a substantial increase in late and necrotic cell populations at 79.7%. The apoptotic outcome of U87MG cells treated with NPs and laser groups (Figure 4D) correlates with the cell viability assay (Figure 4B(ii)) and the intracellular ROS fold increase (Figure 4C), whereby an increment in ROS levels resulted in oxidative stress, resulting in the apoptosis of U87MG cell-treated groups. Evidently, an accumulation of

https://doi.org/10.1021/acsami.3c04696
ACS Appl. Mater. Interfaces 2023, 15, 42153−42169

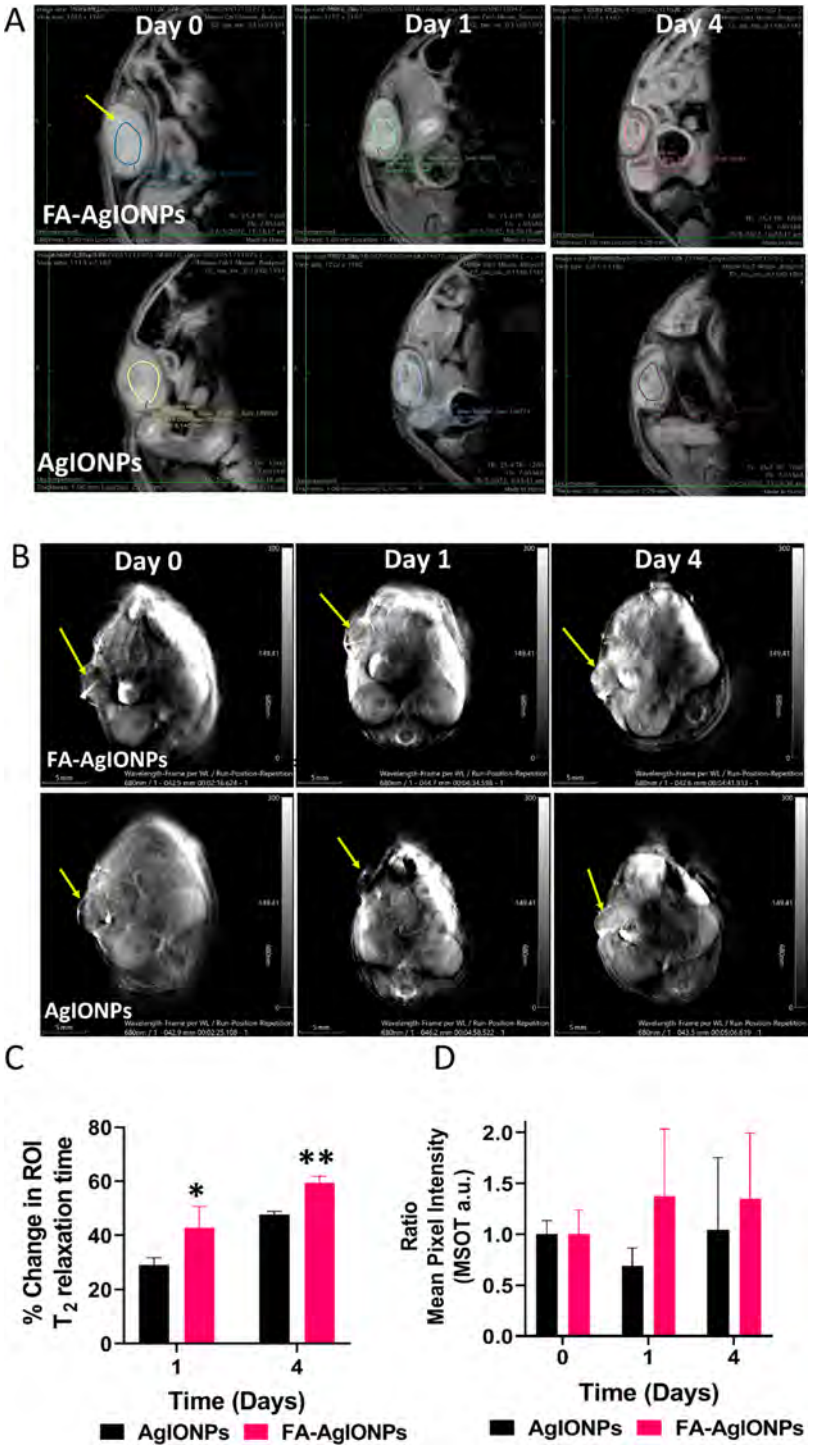

Figure 7. In vivo tumor targeting (MRI T_2 contrast and PAI) of AgIONPs and FA-AgIONPs in U-87 MG tumor-bearing BALB/C mice. Mice were injected intravenously with 10 mg/kg (Ag) NPs with and without FA targeting. Mouse tumors were imaged before (day 0), 1 day, and 4 days post injection of NPs. (A) Representative T_2*-weighted images of mouse tumors using a 7 T MRI. (B) Representative MSOT images. (C) Quantitative analysis of % change in the ROI T_2 relaxation time of tumors injected with AgIONPs and FA-AgIONPs. * Compared to the untargeted group: *p < 0.05, **p < 0.01. (D) Quantitative ratiometric analysis of the MSOT mean pixel intensity at 680 nm from the center of the tumors injected with AgIONPs and FA-AgIONPs.

ROS can activate intrinsic pathways of apoptosis, which leads to the activation of a series of caspases resulting in the cleavage of cellular proteins and cancer cell death by apoptosis.[60] Correspondingly, studies performed by Gurunathan and Vasanth et al. demonstrated that AgNPs generated an increased ROS production, which induced apoptosis and cell death of MDA MB 231 and HeLa cells, respectively.[61,62] Here, our results suggest that combining NPs and laser exposure resulted in further significant synergistic killing and total obliteration of U87MG cells in vitro.

3.5. In Vitro MRI and PAI Imaging of Cells with and without FA. AgIONPs were conjugated with the FA ligand to

https://doi.org/10.1021/acsami.3c04696
ACS Appl. Mater. Interfaces 2023, 15, 42153−42169

target FRα that are substantially expressed in many cancer cells, specifically glioma. Hence, the efficacy of targeting FRα in glioma U87MG cells was evaluated by comparing the uptake of AgIONPs at 4 and 24 h incubation, with (FA-PEG-SH and mPEG-SH) and without FA (only mPEG-SH) targeting in both malignant and nonmalignant cells (CHO cells). Treated cells were then harvested and suspended in 1% agarose gel, transferred in phantom tubes, and imaged with MRI and PAI (Figure 5A–D). In comparison to CHO cells, U87MG cells treated with FA-AgIONPs demonstrated an enhanced uptake of NPs as displayed by the significant hypointense T_2* contrast at both 4 and 24 h incubation (Figure 5A,B). Significantly shorter T_2* relaxation times were ascertained for U87MG cells treated with FA-AgIONPs in contrast to CHO cells. The enhanced uptake of targeted NPs is clearly due to the presence of higher FRα in U87MG cells in comparison to CHO cells, which allowed specific interactions with FA on the NPS, resulting in enhanced T_2* contrast and a shorter relaxation time. Correspondingly, several studies have demonstrated heightened uptake of NPs targeting FRα accompanied by enhanced therapeutic efficacy in various cancer models.[35,37] Similarly, U87MG treated with AgIONPs with and without FA targeting at 4 h incubation demonstrated a substantial difference in the T_2* relaxation time, with shorter T_2* relaxation times acquired for U87MG cells treated with FA-AgIONPs in comparison to without FA targeting. Nonetheless, at 24 h incubation, U87MG cells treated with and without FA targeting displayed less difference in the T_2* relaxation time most probably due to the longer incubation period, which conferred more time for the NPs to be taken up both selectively and passively by the cancer cells. Evidently, these results suggest that the addition of the FA targeting ligand significantly enhances the uptake of NPs in U87MG cells. Correspondingly, in vitro cell phantoms were also assessed using PAI (Figure 5C,D). U87MG cells incubated with FA-AgIONPs presented an enhanced PA signal at 4 and 24 h time points, indicating a significant difference in the uptake of NPs between CHO and U87MG cells (Figure 5D(ii)). This result demonstrates the selective targeting efficiency and corroborates the MRI results (Figure 3C,D).

3.6. In Vivo Biosafety Assessment. The biosafety of the NPs was assessed in C57/BL6J healthy mice. Three doses of NPs were intravenously administered at two concentrations of 5 and 10 mg/kg Ag. Saline was injected into control groups. There was no significant decrease in body weight of mice in all groups during the study (Figure 6A). Twelve days after injection, mice were sacrificed, and major organs and blood serum were collected for biochemical and histology analyses. The relative organ weight was recorded by measuring the organ weight with respect to the total body weight of vital organs including the heart, lungs, liver, kidneys, and spleens in both saline and NP treatment groups. Mice injected with both concentrations of NPs did not display a substantial difference in organ weights except for the liver (Figure 6B). The weight of the liver at both concentrations was slightly heavier than the control group. Hence, liver function markers such as bilirubin, ALT, glucose, and albumin as well as kidney function markers including creatinine, urea, and uric acid were all measured (Figure 6C(i–vii)). In comparison to the control groups, data acquired revealed a slight reduction in ALT and bilirubin levels in treatment groups. However, lower than normal ALT and bilirubin levels are not usually a cause of concern; on the contrary, elevated levels of these analytes indicate hepatic damage. While the glucose level is higher in both treatment groups in contrast to the control group, it is still within a healthy range between 5.2 and 26.9 mmol/L.[63] The concentrations of albumin, creatinine, urea, and uric acid levels were not significantly different between all treatment groups and were within a healthy acceptable range.[64] Histological images of tissues of major organs (heart, lungs, liver, kidneys, and spleen) stained with H&E revealed no noticeable tissue damage, inflammation, or lesion at the highest NP concentration (10 mg/kg of Ag) in comparison to the control group (Figure 6D). Overall, these results suggested that a high concentration of NPs did not affect hepatic or kidney damage accompanied by no obvious toxicity in tissues of other major organs.

3.7. In Vivo Targeting and MRI and PAI Imaging Efficacy. We evaluated the in vivo feasibility of our NPs as a dual-imaging contrast agent and compared the targeting ability of the FA ligand via MRI and MSOT. Using a 7 T MRI system, T_2 contrast was observed in tumors on days 0, 1, and 4 post intravenous injection of targeted and untargeted NPs. First, a discernible reduction in tumor size was observed in the T_2-weighted images of both targeted and nontargeted groups over time, which corroborates the therapeutic efficacy results detailed above of our NPs. The variations in tumor sizes can be visualized on the MR images, thus providing a noninvasive and longitudinal approach to assess therapeutic efficacy. While the data acquired for tumor volume was not calculated using MRI, a previous study has demonstrated the use of MRI to calculate the tumor volume and evaluate treatment ability in an orthotopic glioma model.[65] Also, T_2 contrast was generated in tumors of both FA-targeted and nontargeted NPs in injected mice, indicating that the NPs accumulated in tumors via both passive and receptor-mediated mechanisms (Figure 7A). Passive uptake is most likely achieved through the enhanced permeability and retention effect, also facilitated by the addition of a stealthy PEG ligand, whereby naïve NPs can extravasate through leaky blood vessels and accumulate in the tumor.[66] Nonetheless, there was a significant difference in the T_2 relaxation time between targeted and untargeted groups, reflecting 42.8 and 29% changes in the T_2 relaxation time on days 1 and 59.3 and 47.7% on day 4, respectively, suggesting that FR targeting enhanced the uptake and retention of NPs in tumors in comparison to the nontargeted group (Figure 7C). Interestingly, in the MSOT imaging of the nontargeted group, the background signal at 680 nm measured at the center of the tumor decreased on day 1 and increased back to basal on day 4. Passive nanoparticle accumulation and tumor ablation at the periphery may have changed the oxygen concentration at the center of the tumor, therefore reducing the amount of Hb at the center of the tumor mass and decreasing the endogenous signal at 680 nm. Furthermore, this result may indicate limited nanoparticle permeation and tumor penetration upon administration of nontargeted nanoparticles. Similar to the MRI results, the 680 nm MSOT signal intensity at the center of the tumor increased post administration of the FA-AgIONPs albeit not statistically significant (Figure 7B,D). This is likely due to the variability in the endogenous Hb signal intensity at 680 nm post nanoparticle administration in combination with particle accumulation. This lack of statistical significance highlights the limitations associated with accurately resolving endogenous and exogenous components with significant PA spectral overlap or similarities. The combined MR and MSOT results highlight the importance of multimodal imaging approaches,

https://doi.org/10.1021/acsami.3c04696
ACS Appl. Mater. Interfaces 2023, 15, 42153–42169

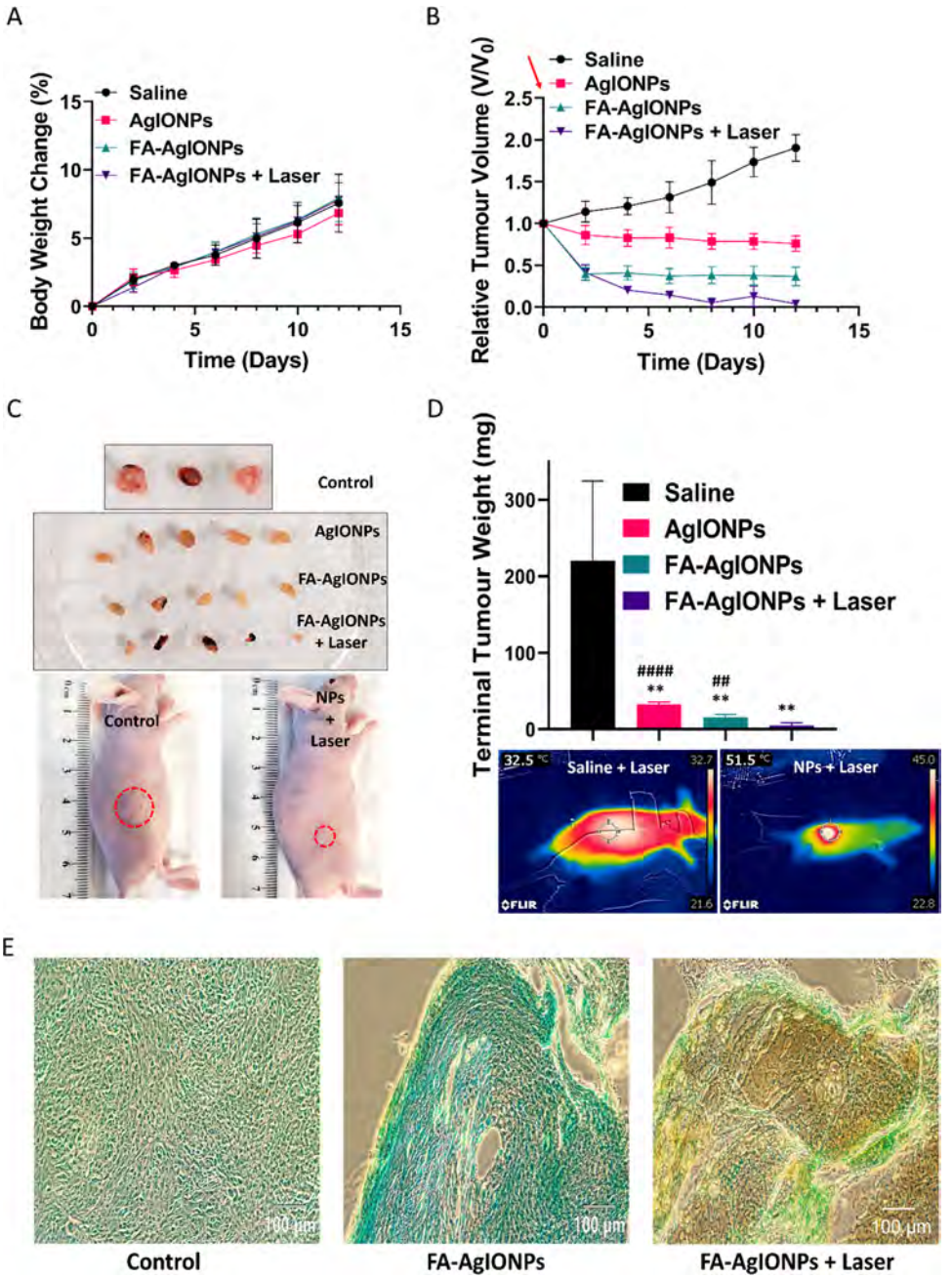

Figure 8. In vivo therapeutic effects of AgIsONPs with and without FA targeting and laser irradiation at (1.5 W/cm^2, 5 min) in U-87 MG tumor-bearing BALB/C mice. Mice were injected intravenously with saline (control group), AgIONPs, and FA-AgIONPs once. (A) Average body weight of mice was monitored twice a week during the treatment. Mice body weight analyzed with repeated measures one-way ANOVA with Tukey's multiple comparisons demonstrated no significant changes in all treatment groups across the experimental period. (B) Changes in tumor volume during the experiment period. Relative tumor volume was defined as the tumor volume (V) measured normalized to the tumor volume on day 0 before administration of treatment (V_0). The red arrow denotes initiation of injection of NPs (10 mg/kg Ag). (C) Images of tumors harvested on day 12 post administration of NPs and representative images of mice treated with saline and NPs + laser. (D) Terminal tumor weight and representative thermal images of mice after laser exposure. * Compared to saline: $^{**}p < 0.01$, $^{***}p < 0.001$, $^{****}p < 0.0001$. # Compared to FA-AgIONPs + laser: $^{\#\#}p < 0.01$, $^{\#\#\#}p < 0.001$, $^{\#\#\#}p < 0.0001$. (E) Histological images of tumor tissues stained with TUNEL.

whereby limitations associated with individual techniques can be overcome.[19] This approach encompasses the development of multifunctional NPs, whereby complementary roles of each technique can be fully exploited.

3.8. In Vivo Therapeutic and Photothermal Efficacy. Due to the great performance of the NPs in tumor targeting and imaging in vivo, the NPs were applied for tumor thermo-chemotherapy. There are three treatment groups comprising intravenous injection of AgIONPs only, FA-AgIONPs only, and FA-AgIONPs plus laser irradiation. The in vivo therapeutic efficacies of these three groups in the U87MG tumor model were compared with the control (saline-injected). Each therapeutic group contained five mice. Upon reaching an average tumor volume of >100 mm^3, mice were intravenously injected with 10 mg/kg NPs. Twenty-four hours post injection of FA-AgIONPs, the tumors from the laser

https://doi.org/10.1021/acsami.3c04696
ACS Appl. Mater. Interfaces 2023, 15, 42153−42169

groups were irradiated with an 808 nm laser, at a power of 1.5 W/cm^2 for 5 min, and temperature changes were recorded with a thermal camera. The body weights and tumor sizes of all four groups of mice were recorded every 2 days during the period of experiments. There was no distinct difference in body weight between all groups, implying that NPs and laser exposure resulted in no apparent toxicity (Figure 8A). While the tumor volume continued to grow over time in the saline-treated group, all other treatment groups displayed a substantial reduction in tumor growth in comparison to controls (Figure 8B,C). Notably, FA-targeted NPs resulted in an enhanced reduction in tumor volume as depicted by the terminal tumor weight (Figure 8D) in comparison to the untargeted treatment group, clearly suggesting the relevance and improved therapeutic efficacy of incorporating FA targeting in treating U87MG tumors. Importantly, the combination of FA-targeted NPS and photothermal laser induced a temperature elevation until an average of 48.2 °C and resulted in further significant synergistic reduction in tumor volume and weight (Figure 8B−D). Notably, this acquired temperature increment was well above the threshold (43 °C) required for irreversible tumor cell damage, which led to a remarkable shrinkage in tumor size. Interestingly, a study by Chen et al. reported that repeated intravenous administration of gold nanoparticles (75 mg/kg) loaded with Doxorubicin resulted in a substantial reduction in S180 tumors in vivo upon laser irradiation at 1 W/cm^2 for 10 min.[67] This therapeutic outcome is achieved based on four cycles of tail vein injection and laser exposure.[67] Another study by He and co-workers established the efficacy of one systemic administration of titanium nitride NPs as successful anticancer PTT agents in a HeLa mice model.[44] However, this study not only utilized a very high concentration of NPs at 20 mg/kg but tumors were also exposed to a high laser irradiation strength of 2 W/cm^2 for 10 min.[44] Hence, it should be highlighted that our FA-AgIONP (10 mg/kg) displayed potent photothermal tumor ablation with just one intravenous dose and one cycle of laser exposure at 1.5 W/cm^2 for 5 min, clearly indicating its outstanding anticancer capabilities. The areas surrounding the tumor were devoid of burns, suggesting that the laser exposure did not affect the surrounding tissues (based on the visual outlook of the region surrounding the tumor).[68,69] The temperature in the tumors of mice injected with saline and exposed to laser reached a maximum of 35 °C, which was inadequate to cause irrevocable tumor damage.[68] Hence, the temperature attained in the NP + laser group reached an average of 13.2 °C higher than that in the control group, suggesting the significant accumulation and efficient photothermal ability of our NPs (Figure 8D).

As shown in Figure 8E, tumors stained with TUNEL in the control group demonstrated a green fluorescence devoid of brown stains with a healthy and confluent cell morphology. Upon treatment with NPs, cancer cells appeared to have shrunk, accompanied by condensed chromatin, a hallmark of cells undergoing stress in the early stages of apoptosis.[70] The addition of laser irradiation resulted in distinct brown stains representing DNA fragmentations and nuclear collapse, which occurs in late-stage apoptosis. Hence, the results obtained correlate with the in vitro quantification of the apoptotic cell population of U87MG cells treated with NPs and laser exposure (Figure 5D). Recently, Kim et al. have demonstrated the photothermal treatment application of AgNPs in the NIR based on the effective inhibition of melanoma cells' proliferation in vitro via induction of ROS. Nonetheless, this study did not proceed to display the efficacy of NPs as PTT agents in vivo nor demonstrated their imaging ability.[14] Here, these findings demonstrated that FA-AgIONPs in combination with laser irradiation present a safe and powerful strategy as an anticancer photothermal therapy in vivo.

4. CONCLUSIONS

We have successfully developed a novel multifunctional and targeted AgIONP which was tuned for NIR wavelength absorption and application in photothermal treatment, along with dual-imaging efficacy using MRI (both in vitro and in vivo) and MSOT (in vitro). While there are some reports on the nanocomposites of silver and iron oxide, we are the first to develop and report silver-coated iron oxide nanoparticles that have strong absorbance in the near-infrared (NIR) range, allowing photothermal therapy triggered by NIR laser. This is a great advantage of our NPs. In the literature, silver nanoparticles have been employed for photothermal therapy, but visible laser was used, which does not have deep tissue penetration capability. While gold-coated iron oxide nanoparticles have been developed to provide NIR photothermal therapy, they could not offer simultaneous chemotherapy like those of our spiky AgIONPs. Our novel spiky AgIONPs could effectively induce cancer cell death, even by themselves (without laser application).

Targeting folate receptors on cancer cells significantly boosted the cytotoxicity of NPs, and the combination of photothermal laser resulted in further significant synergistic killing of U87MG tumors both in vitro and in vivo. Additionally, in vitro phantoms imaged with MRI and MSOT accompanied by in vivo MRI imaging studies displayed preferential uptake of folate-targeted NPs in U87MG tumors representing the selective targeting ability of NPs. Importantly, the biosafety and biochemical analysis of NPs demonstrated no obvious toxicity in vivo. Overall, our FA-AgIONPs exhibited excellent potential in simultaneous application for a safe and successful targeted photothermal treatment and bimodal imaging of a cancer model using MRI in vivo and MSOT in vitro. Especially, our nanohybrid material could mostly eliminate the tumors after 12 days with only a single injection (dose), demonstrating its excellent anticancer performance. The potential application of this new nanohybrid is not limited to theranostics of cancers but could be expanded to other diseases, such as thrombosis and infectious diseases.

■ ASSOCIATED CONTENT

Data Availability Statement

The raw/processed data required to reproduce these findings are available upon request.

Supporting Information

The Supporting Information is available free of charge at https://pubs.acs.org/doi/10.1021/acsami.3c04696.

TEM images, ζ potential, photothermal conversion efficiency calculation, flow cytometry analysis, characterization of NPs, optimization of folic acid conjugation to NPs, and stability of complete NPs in PBS (PDF)

■ AUTHOR INFORMATION

Corresponding Author

Hang Thu Ta − *Queensland Micro- and Nanotechnology Centre, Griffith University, Nathan 4111, Australia; School*

https://doi.org/10.1021/acsami.3c04696
ACS Appl. Mater. Interfaces 2023, 15, 42153−42169

of Environment and Science, Griffith University, Nathan 4111 Queensland, Australia; Australian Institute for Bioengineering and Nanotechnology, University of Queensland, Nathan 4111, Australia; orcid.org/0000-0003-1188-0472; Email: h.ta@griffith.edu.au

Authors

Shehzahdi S. Moonshi − *Queensland Micro- and Nanotechnology Centre, Griffith University, Nathan 4111, Australia; School of Environment and Science, Griffith University, Nathan 4111 Queensland, Australia;* orcid.org/0000-0003-2048-595X

Karla X. Vazquez-Prada − *Queensland Micro- and Nanotechnology Centre, Griffith University, Nathan 4111, Australia; Australian Institute for Bioengineering and Nanotechnology, University of Queensland, Nathan 4111, Australia*

Joyce Tang − *Queensland Micro- and Nanotechnology Centre, Griffith University, Nathan 4111, Australia; School of Environment and Science, Griffith University, Nathan 4111 Queensland, Australia*

Nicholas J. Westra van Holthe − *Australian Institute for Bioengineering and Nanotechnology, University of Queensland, Nathan 4111, Australia; National Imaging Facility, Centre for Advanced Imaging, University of Queensland, Brisbane 4072, Australia;* orcid.org/0000-0002-0076-2967

Gary Cowin − *National Imaging Facility, Centre for Advanced Imaging, University of Queensland, Brisbane 4072, Australia*

Yuao Wu − *Queensland Micro- and Nanotechnology Centre, Griffith University, Nathan 4111, Australia; School of Environment and Science, Griffith University, Nathan 4111 Queensland, Australia*

Huong D. N. Tran − *Queensland Micro- and Nanotechnology Centre, Griffith University, Nathan 4111, Australia; Australian Institute for Bioengineering and Nanotechnology, University of Queensland, Nathan 4111, Australia*

Ryan Mckinnon − *School of Pharmacy and Medical Sciences, Griffith University, Gold Coast 4222, Australia*

Andrew C. Bulmer − *School of Pharmacy and Medical Sciences, Griffith University, Gold Coast 4222, Australia*

Complete contact information is available at: https://pubs.acs.org/10.1021/acsami.3c04696

Author Contributions

S.S.M.: Investigation, formal analysis, interpretation of data, writing—original draft, visualization. K.X.V.-P.: Investigation, formal analysis. J.T.: Investigation. N.J.W.v.H.: Investigation, formal analysis, writing—review. G.C.: Investigation. Y.W.: Investigation. H.D.N.T.: Investigation. R.M.: Investigation. A.C.B.: Investigation and resources. H.T.T.: Conceptualization, methodology, supervision, resources, writing—review and editing, project administration, funding acquisition.

Notes

The authors declare no competing financial interest.

■ ACKNOWLEDGMENTS

This work was funded by the National Health and Medical Research Council (H.T.T.: APP1037310, APP1182347, APP2002827). K.V.P. and H.D.N.T. are supported by PhD scholarships from the University of Queensland. H.T.T. is supported by a Heart Foundation Future Leader Fellowship (102761). The authors would like to acknowledge the Australian National Fabrication Facility (Queensland Node) for providing access to key items of equipment. The authors acknowledge the facilities and scientific and technical assistance of the National Imaging Facility, a National Collaborative Research Infrastructure Strategy (NCRIS) capability, at the Centre for Advanced Imaging and School of Chemistry and Molecular Biosciences University of Queensland.

■ REFERENCES

(1) Yan, H.; Shang, W.; Sun, X.; Zhao, L.; Wang, X.; Zhang, S.; Xu, N.; Xu, W.; Tian, J.; Kang, F. Neoadjuvant Nano-Photothermal Therapy used Before Operation Effectively Assists in Surgery for Breast Cancer. *Nanoscale* **2019**, *11* (2), 706−716.

(2) Xie, Y.-H.; Chen, Y.-X.; Fang, J.-Y. Comprehensive Review of Targeted Therapy for Colorectal Cancer. *Signal Transduction Targeted Ther.* **2020**, *5* (1), 22.

(3) Vasan, N.; Baselga, J.; Hyman, D. M. A View on Drug Resistance in Cancer. *Nature* **2019**, *575* (7782), 299−309.

(4) Chu, Z.; Wang, Z.; Chen, L.; Wang, X.; Huang, C.; Cui, M.; Yang, D.-P.; Jia, N. Combining Magnetic Resonance Imaging with Photothermal Therapy of CuS@BSA Nanoparticles for Cancer Theranostics. *ACS Appl. Nano Mater.* **2018**, *1* (5), 2332−2340.

(5) Phan, T. T. V.; Bui, N. Q.; Cho, S.-W.; Bharathiraja, S.; Manivasagan, P.; Moorthy, M. S.; Mondal, S.; Kim, C.-S.; Oh, J. Photoacoustic Imaging-Guided Photothermal Therapy with Tumor-Targeting HA-FeOOH@PPy Nanorods. *Sci. Rep.* **2018**, *8* (1), No. 8809.

(6) Cao, H.; Zou, L.; He, B.; Zeng, L.; Huang, Y.; Yu, H.; Zhang, P.; Yin, Q.; Zhang, Z.; Li, Y. Albumin Biomimetic Nanocorona Improves Tumor Targeting and Penetration for Synergistic Therapy of Metastatic Breast Cancer. *Adv. Funct. Mater.* **2017**, *27* (11), No. 1605679.

(7) Yan, F.; Duan, W.; Li, Y.; Wu, H.; Zhou, Y.; Pan, M.; Liu, H.; Liu, X.; Zheng, H. NIR-Laser-Controlled Drug Release from DOX/IR-780-Loaded Temperature-Sensitive-Liposomes for Chemo-Photothermal Synergistic Tumor Therapy. *Theranostics* **2016**, *6* (13), 2337−2351.

(8) Rehman, A. u.; Wu, Y.; Tran, H. D. N.; Vazquez-Prada, K.; Liu, Y.; Adelnia, H.; Kurniawan, N. D.; Anjum, M. N.; Moonshi, S. S.; Ta, H. T. Silver/Iron Oxide Nano-Popcorns for Imaging and Therapy. *ACS Appl. Nano Mater.* **2021**, *4*, 10136−10147, DOI: 10.1021/acsanm.1c01571.

(9) Fithri, N. A.; Wu, Y.; Cowin, G.; Akther, F.; Tran, H. D. N.; Tse, B.; van Holthe, N. W.; Moonshi, S. S.; Peter, K.; Wang, X.; Truong, N. P.; Ta, H. T. Gold-Iron Oxide Nanoparticle: A Unique Multimodal Theranostic Approach for Thrombosis. *Appl. Mater. Today* **2023**, *31*, No. 101750.

(10) Zainuddin, N. A. M.; Ariannejad, M. M.; Arasu, P. T.; Harun, S. W.; Zakaria, R. Investigation of Cladding Thicknesses on Silver SPR based Side-Polished Optical Fiber Refractive-Index Sensor. *Results Phys.* **2019**, *13*, No. 102255.

(11) Shipunova, V. O.; Belova, M. M.; Kotelnikova, P. A.; Shilova, O. N.; Mirkasymov, A. B.; Danilova, N. V.; Komedchikova, E. N.; Popovtzer, R.; Deyev, S. M.; Nikitin, M. P. Photothermal Therapy with HER2-Targeted Silver Nanoparticles Leading to Cancer Remission. *Pharmaceutics* **2022**, *14*, 1013.

(12) Bejot, R.; Goggi, J.; Moonshi, S. S.; Padmanabhan, P.; Bhakoo, K. K. Aminooxy-Functionalized DOTA for Radiolabeling of Oxidized Antibodies: Evaluation of Site-Specific 111In-Labeled Trastuzumab. *J. Labelled Compd. Radiopharm.* **2012**, *55* (9), 346−353.

(13) Lv, Z.; He, S.; Wang, Y.; Zhu, X. Noble Metal Nanomaterials for NIR-Triggered Photothermal Therapy in Cancer. *Adv. Healthcare Mater.* **2021**, *10* (6), No. 2001806.

(14) Kim, D.; Amatya, R.; Hwang, S.; Lee, S.; Min, K. A.; Shin, M. C. BSA-Silver Nanoparticles: A Potential Multimodal Therapeutics for Conventional and Photothermal Treatment of Skin Cancer.

Pharmaceutics **2021**, *13*, No. 575, DOI: 10.3390/pharmaceutics13040575.
(15) Ye, J.; Fu, G.; Yan, X.; Liu, J.; Wang, X.; Cheng, L.; Zhang, F.; Sun, P. Z.; Liu, G. Noninvasive Magnetic Resonance/Photoacoustic Imaging for Photothermal Therapy Response Monitoring. *Nanoscale* **2018**, *10* (13), 5864−5868.
(16) Moonshi, S. S.; Wu, Y.; Ta, H. T. Visualizing Stem Cells in vivo Using Magnetic Resonance Imaging. *Wiley Interdiscip. Rev.: Nanomed. Nanobiotechnol.* **2022**, *14* (2), No. e1760.
(17) Wu, Y.; Zhang, R.; Tran, H. D.; Kurniawan, N. D.; Moonshi, S. S.; Whittaker, A. K.; Ta, H. T. Chitosan Nanococktails Containing Both Ceria and Superparamagnetic Iron Oxide Nanoparticles for Reactive Oxygen Species-Related Theranostics. *ACS Appl. Nano Mater.* **2021**, *4* (4), 3604−3618.
(18) Wu, Y.; Cowin, G.; Moonshi, S. S.; Tran, H. D. N.; Fithri, N. A.; Whittaker, A. K.; Zhang, R.; Ta, H. T. Engineering Chitosan Nano-Cocktail Containing Iron Oxide and Ceria: A Two-In-One Approach for Treatment of Inflammatory Diseases and Tracking of Material Delivery. *Mater. Sci. Eng., C* **2021**, *131*, No. 112477.
(19) Moonshi, S. S.; Wu, Y.; Ta, H. T. Visualizing stem cells in vivo using magnetic resonance imaging. *Wiley Interdiscip. Rev.: Nanomed. Nanobiotechnol.* **2022**, *14* (2), No. e1760.
(20) Vazquez-Prada, K. X.; Lam, J.; Kamato, D.; Xu, Z. P.; Little, P. J.; Ta, H. T. Targeted Molecular Imaging of Cardiovascular Diseases by Iron Oxide Nanoparticles. *Arterioscler., Thromb., Vasc. Biol.* **2021**, *41* (2), 601−613.
(21) Ta, H. T.; Li, Z.; Hagemeyer, C. E.; Cowin, G.; Zhang, S.; Palasubramaniam, J.; Alt, K.; Wang, X.; Peter, K.; Whittaker, A. K. Molecular Imaging of Activated Platelets via Antibody-Targeted Ultra-Small Iron Oxide Nanoparticles Displaying Unique Dual MRI Contrast. *Biomaterials* **2017**, *134*, 31−42.
(22) Wu, Y.; Yang, Y.; Zhao, W.; Xu, Z. P.; Little, P. J.; Whittaker, A. K.; Zhang, R.; Ta, H. T. J. J. o. M. C. B. Novel Iron Oxide−Cerium Oxide Core−Shell Nanoparticles as A Potential Theranostic Material for ROS Related Inflammatory Diseases. *J. Mater. Chem. B* **2018**, *6* (30), 4937−4951.
(23) Ta, H. T.; Arndt, N.; Wu, Y.; Lim, H. J.; Landeen, S.; Zhang, R.; Kamato, D.; Little, P. J.; Whittaker, A. K.; Xu, Z. P. J. N. Activatable Magnetic Resonance Nanosensor as a Potential Imaging Agent for Detecting and Discriminating Thrombosis. *Nanoscale* **2018**, *10* (31), 15103−15115.
(24) Yusof, N. N. M.; McCann, A.; Little, P. J.; Ta, H. T. Non-Invasive Imaging Techniques for the Differentiation of Acute and Chronic Thrombosis. *Thromb Res.* **2019**, *177*, 161−171.
(25) Liu, Y.; Wu, Y.; Zhang, R.; Lam, J.; Ng, J. C.; Xu, Z. P.; Li, L.; Ta, H. T. J. A. A. B. M. Investigating the Use of Layered Double Hydroxide Nanoparticles as Carriers of Metal Oxides for Theranostics of ROS-related Diseases. *ACS Appl. Bio Mater.* **2019**, *2* (12), 5930−5940.
(26) Arndt, N.; Tran, H. D. N.; Zhang, R.; Xu, Z. P.; Ta, H. T. Different Approaches to Develop Nanosensors for Diagnosis of Diseases. *Adv. Sci.* **2020**, *7* (24), No. 2001476.
(27) Wu, Y.; Vazquez-Prada, K. X.; Liu, Y.; Whittaker, A. K.; Zhang, R.; Ta, H. T. Recent Advances in the Development of Theranostic Nanoparticles for Cardiovascular Diseases. *Nanotheranostics* **2021**, *5* (4), 499−514.
(28) Zhang, Y.; Koradia, A.; Kamato, D.; Popat, A.; Little, P. J.; Ta, H. T. Treatment of Atherosclerotic Plaque: Perspectives on Theranostics. *J. Pharm. Pharmacol.* **2019**, *71* (7), 1029−1043.
(29) Ta, H. T.; Prabhu, S.; Leitner, E.; Jia, F.; von Elverfeldt, D.; Jackson, K. E.; Heidt, T.; Nair, A. K.; Pearce, H.; von Zur Muhlen, C.; Wang, X.; Peter, K.; Hagemeyer, C. E. Enzymatic Single-Chain Antibody Tagging: A Universal Approach to Targeted Molecular Imaging and Cell Homing in Cardiovascular Disease. *Circ. Res.* **2011**, *109* (4), 365−73.
(30) Wu, W.; Wu, Z.; Yu, T.; Jiang, C.; Kim, W. S. Recent Progress on Magnetic Iron Oxide Nanoparticles: Synthesis, Surface Functional Strategies and Biomedical Applications. *Sci. Technol. Adv. Mater.* **2015**, *16* (2), No. 023501.
(31) Tran, H. D. N.; Moonshi, S. S.; Xu, Z. P.; Ta, H. T. Influence of Nanoparticles on the Haemostatic Balance: Between Thrombosis and Haemorrhage. *Biomater. Sci.* **2021**, *10* (1), 10−50.
(32) Tang, J. L. Y.; Moonshi, S. S.; Ta, H. T. Nanoceria: An Innovative Strategy for Cancer Treatment. *Cell. Mol. Life Sci.* **2023**, *80* (2), No. 46.
(33) Boogerd, L. S. F.; Boonstra, M. C.; Beck, A.-J.; Charehbili, A.; Hoogstins, C. E. S.; Prevoo, H. A. J. M.; Singhal, S.; Low, P. S.; van de Velde, C. J. H.; Vahrmeijer, A. L. Concordance of Folate Receptor-α Expression between Biopsy, Primary Tumor and Metastasis in Breast Cancer and Lung Cancer Patients. *Oncotarget* **2016**, *7* (No 14), No. 17442, DOI: 10.18632/oncotarget.7856.
(34) Cheung, A.; Bax, H. J.; Josephs, D. H.; Ilieva, K. M.; Pellizzari, G.; Opzoomer, J.; Bloomfield, J.; Fittall, M.; Grigoriadis, A.; Figini, M.; Canevari, S.; Spicer, J. F.; Tutt, A. N.; Karagiannis, S. N. Targeting Folate Receptor Alpha for Cancer Treatment. *Oncotarget* **2016**, *7* (32), 52553−52574.
(35) Fasehee, H.; Dinarvand, R.; Ghavamzadeh, A.; Esfandyari-Manesh, M.; Moradian, H.; Faghihi, S.; Ghaffari, S. H. Delivery of Disulfiram into Breast Cancer Cells using Folate-Receptor-Targeted PLGA-PEG Nanoparticles: in vitro and in vivo Investigations. *J. Nanobiotechnol.* **2016**, *14* (1), No. 32.
(36) Elechalawar, C. K.; Bhattacharya, D.; Ahmed, M. T.; Gora, H.; Sridharan, K.; Chaturbedy, P.; Sinha, S. H.; Chandra Sekhar Jaggarapu, M. M.; Narayan, K. P.; Chakravarty, S.; Eswaramoorthy, M.; Kundu, T. K.; Banerjee, R. Dual Targeting of Folate Receptor-Expressing Glioma Tumor-Associated Macrophages and Epithelial Cells in the Brain Using a Carbon Nanosphere−Cationic Folate Nanoconjugate. *Nanoscale Adv.* **2019**, *1* (9), 3555−3567.
(37) Agrawal, U.; Chashoo, G.; Sharma, P. R.; Kumar, A.; Saxena, A. K.; Vyas, S. P. Tailored Polymer−Lipid Hybrid Nanoparticles for the Delivery of Drug Conjugate: Dual Strategy for Brain Targeting. *Colloids Surf., B* **2015**, *126*, 414−425.
(38) McCord, E.; Pawar, S.; Koneru, T.; Tatiparti, K.; Sau, S.; Iyer, A. K. Folate Receptors' Expression in Gliomas May Possess Potential Nanoparticle-Based Drug Delivery Opportunities. *ACS Omega* **2021**, *6* (6), 4111−4118.
(39) Vazquez-Prada, K. X.; Moonshi, S. S.; Wu, Y.; Akther, F.; Tse, B. W. C.; Sokolowski, K. A.; Peter, K.; Wang, X.; Xu, G.; Ta, H. T. A Spiky Silver-Iron Oxide Nanoparticle for Highly Efficient Targeted Photothermal Therapy and Multimodal Imaging of Thrombosis. *Small* **2023**, *19*, No. e2205744.
(40) Houtmeyers, A.; Duchateau, L.; Grünewald, B.; Hermans, K. Reference Intervals for Biochemical Blood Variables, Packed Cell Volume, and Body Temperature in Pet Rats (Rattus Norvegicus) using Point-of-Care Testing. *Vet. Clin. Pathol.* **2016**, *45* (4), 669−679.
(41) Cañamares, M. V.; Garcia-Ramos, J. V.; Gómez-Varga, J. D.; Domingo, C.; Sanchez-Cortes, S. Comparative Study of the Morphology, Aggregation, Adherence to Glass, and Surface-Enhanced Raman Scattering Activity of Silver Nanoparticles Prepared by Chemical Reduction of Ag+ Using Citrate and Hydroxylamine. *Langmuir* **2005**, *21* (18), 8546−53.
(42) Hien Pham, T. T.; Cao, C.; Sim, S. J. Application of Citrate-Stabilized Gold-Coated Ferric Oxide Composite Nanoparticles for Biological Separations. *J. Magn. Magn. Mater.* **2008**, *320* (15), 2049−2055.
(43) Amendola, V.; Pilot, R.; Frasconi, M.; Maragò, O. M.; Iatì, M. A. Surface Plasmon Resonance in Gold Nanoparticles: A Review. *J. Phys.: Condens. Matter* **2017**, *29* (20), No. 203002.
(44) He, W.; Ai, K.; Jiang, C.; Li, Y.; Song, X.; Lu, L. Plasmonic Titanium Nitride Nanoparticles for in vivo Photoacoustic Tomography Imaging and Photothermal Cancer Therapy. *Biomaterials* **2017**, *132*, 37−47.
(45) Chen, Y.; Ai, K.; Liu, J.; Sun, G.; Yin, Q.; Lu, L. Multifunctional Envelope-Type Mesoporous Silica Nanoparticles for pH-Responsive Drug Delivery and Magnetic Resonance Imaging. *Biomaterials* **2015**, *60*, 111−20.
(46) Xiao, K.; Li, Y.; Luo, J.; Lee, J. S.; Xiao, W.; Gonik, A. M.; Agarwal, R. G.; Lam, K. S. The Effect of Surface Charge on in vivo

Biodistribution of PEG-Oligocholic Acid based Micellar Nanoparticles. *Biomaterials* **2011**, *32* (13), 3435−3446.
(47) Vieira, M. E. M.; Silva, M. L. S. e.; Oliveira, L. F. C. d.; Perrone, Í. T.; Stephani, R. X-ray Energy Dispersive Spectroscopy (EDS) Coupled with Scanning Electron Microscope (SEM): Fundamentals and Applications in Dairy Products. *Res., Soc., Dev.* **2021**, *10* (10), No. e262101018622.
(48) Li, Z.; Huang, H.; Tang, S.; Li, Y.; Yu, X.-F.; Wang, H.; Li, P.; Sun, Z.; Zhang, H.; Liu, C.; Chu, P. K. Small Gold Nanorods Laden Macrophages for Enhanced Tumor Coverage in Photothermal Therapy. *Biomaterials* **2016**, *74*, 144−154.
(49) Zhao, L.; Zhang, X.; Wang, X.; Guan, X.; Zhang, W.; Ma, J. Recent Advances in Selective Photothermal Therapy of Tumor. *J. Nanobiotechnol.* **2021**, *19* (1), No. 335.
(50) Cheng, M.; Zhang, Y.; Zhang, X.; Wang, W.; Yuan, Z. One-Pot Synthesis of Acid-Induced in situ Aggregating Theranostic Gold Nanoparticles with Enhanced Retention in Tumor Cells. *Biomater. Sci.* **2019**, *7* (5), 2009−2022.
(51) Taruttis, A.; Ntziachristos, V. Advances in Real-Time Multispectral Optoacoustic Imaging and Its Applications. *Nat. Photonics* **2015**, *9* (4), 219−227.
(52) Fuenzalida Werner, J. P.; Huang, Y.; Mishra, K.; Janowski, R.; Vetschera, P.; Heichler, C.; Chmyrov, A.; Neufert, C.; Niessing, D.; Ntziachristos, V.; Stiel, A. C. Challenging a Preconception: Optoacoustic Spectrum Differs from the Optical Absorption Spectrum of Proteins and Dyes for Molecular Imaging. *Anal. Chem.* **2020**, *92* (15), 10717−10724.
(53) Yang, T.; Tang, Ya.; Liu, L.; Lv, X.; Wang, Q.; Ke, H.; Deng, Y.; Yang, H.; Yang, X.; Liu, G.; Zhao, Y.; Chen, H. Size-Dependent Ag2S Nanodots for Second Near-Infrared Fluorescence/Photoacoustics Imaging and Simultaneous Photothermal Therapy. *ACS Nano* **2017**, *11* (2), 1848−1857.
(54) Garcia, M. A. Surface Plasmons in Metallic Nanoparticles: Fundamentals and Applications. *J. Phys. D: Appl. Phys.* **2012**, *45* (38), No. 389501.
(55) Ledermann, J. A.; Canevari, S.; Thigpen, T. Targeting the Folate Receptor: Diagnostic and Therapeutic Approaches to Personalize Cancer Treatments. *Ann. Oncol.* **2015**, *26* (10), 2034−2043.
(56) Viola-Villegas, N.; Vortherms, A.; Doyle, R. P. Targeting Gallium to Cancer Cells through the Folate Receptor. *Drug Target Insights* **2008**, *3*, DTI.S651.
(57) Kamen, B. A.; Smith, A. K.; Phillips, M.; Grasso, L.; Farletuzumab, A. Monoclonal Antibody against Folate Receptor Alpha (FRα), Does not Block Folate or Anti-Folate Binding or Alter Drug Potency Assessed in vitro. *J. Clin. Oncol.* **2011**, *29* (15_suppl), e13544.
(58) Kim, D.; Kim, H. Induction of Apoptotic Temperature in Photothermal Therapy under Various Heating Conditions in Multi-Layered Skin Structure. *Int. J. Mol. Sci.* **2021**, *22* (20), No. 11091, DOI: 10.3390/ijms222011091.
(59) Reczek, C. R.; Chandel, N. S. The Two Faces of Reactive Oxygen Species in Cancer. *Annu. Rev. Cancer Biol.* **2017**, *1* (1), 79−98.
(60) Perillo, B.; Di Donato, M.; Pezone, A.; Di Zazzo, E.; Giovannelli, P.; Galasso, G.; Castoria, G.; Migliaccio, A. ROS in Cancer Therapy: the Bright Side of the Moon. *Exp. Mol. Med.* **2020**, *52* (2), 192−203.
(61) Vasanth, K.; Ilango, K.; MohanKumar, R.; Agrawal, A.; Dubey, G. P. Anticancer Activity of Moringa Oleifera Mediated Silver Nanoparticles on Human Cervical Carcinoma Cells by Apoptosis Induction. *Colloids Surf., B* **2014**, *117*, 354−359.
(62) Gurunathan, S.; Raman, J.; Abd Malek, S. N.; John, P. A.; Vikineswary, S. Green Synthesis of Silver Nanoparticles using Ganoderma Neo-Japonicum Imazeki: A Potential Cytotoxic Agent against Breast Cancer Cells. *Int. J. Nanomed.* **2013**, *8*, 4399−4413.
(63) Otto, G. P.; Rathkolb, B.; Oestereicher, M. A.; Lengger, C. J.; Moerth, C.; Micklich, K.; Fuchs, H.; Gailus-Durner, V.; Wolf, E.; Hrabě de Angelis, M. Clinical Chemistry Reference Intervals for C57BL/6J, C57BL/6N, and C3HeB/FeJ Mice (Mus musculus). *J. Am. Assoc Lab Anim Sci.* **2016**, *55* (4), 375−386.
(64) Silva-Santana, G.; Bax, J. C.; Fernandes, D. C. S.; Bacellar, D. T. L.; Hooper, C.; Dias, A. A. S. O.; Silva, C. B.; de Souza, A. M.; Ramos, S.; Santos, R. A.; Pinto, T. R.; Ramão, M. A.; Mattos-Guaraldi, A. L. Clinical Hematological and Biochemical Parameters in Swiss, BALB/c, C57BL/6 and B6D2F1Mus Musculus. *Anim. Models Exp. Med.* **2020**, *3* (4), 304−315.
(65) Moonshi, S. S.; Bejot, R.; Atcha, Z.; Vijayaragavan, V.; Bhakoo, K. K.; Goggi, J. L. A Comparison of PET Imaging Agents for the Assessment of Therapy Efficacy in a Rodent Model of Glioma. *Am. J. Nucl. Med. Mol. Imaging* **2013**, *3* (5), 397−407.
(66) Subhan, M. A.; Yalamarty, S. S. K.; Filipczak, N.; Parveen, F.; Torchilin, V. P. Recent Advances in Tumor Targeting via EPR Effect for Cancer Treatment. *J. Pers Med.* **2021**, *11* (6), No. 571, DOI: 10.3390/jpm11060571.
(67) Chen, H.; Zhang, X.; Dai, S.; Ma, Y.; Cui, S.; Achilefu, S.; Gu, Y. Multifunctional Gold Nanostar Conjugates for Tumor Imaging and Combined Photothermal and Chemo-Therapy. *Theranostics* **2013**, *3* (9), 633−49.
(68) Yuan, A.; Qiu, X.; Tang, X.; Liu, W.; Wu, J.; Hu, Y. Self-Assembled PEG-IR-780-C13 Micelle as A Targeting, Safe and Highly-Effective Ehotothermal Agent for in vivo Imaging and Cancer Therapy. *Biomaterials* **2015**, *51*, 184−193.
(69) Cao, Y.; Ren, Q.; Hao, R.; Sun, Z. Innovative Strategies to Boost Photothermal Therapy at Mild Temperature Mediated by Functional Nanomaterials. *Mater. Des.* **2022**, *214*, No. 110391.
(70) Saraste, A.; Pulkki, K. Morphologic and Biochemical Hallmarks of Apoptosis. *Cardiovasc. Res.* **2000**, *45* (3), 528−537.

Supporting Information

Spiky Silver-Iron Oxide NanoHybrid for Effective Dual-Imaging and Synergistic Thermo-Chemotherapy

Shehzahdi S. Moonshi[1,2], Karla X. Vazquez-Prada[1,3], Joyce Tang[1,2], Nicholas J. Westra van Holthe[3,4], Gary Cowin[4], Yuao Wu[1,2], Huong D.N. Tran[1,3], Ryan Mckinnon[5], Andrew C. Bulmer[5], Hang Thu Ta[1,2,3*]

[1] Queensland Micro- and Nanotechnology Centre, Griffith University, Australia

[2] School of Environment and Science, Griffith University, Queensland, Australia.

[3]Australian Institute for Bioengineering and Nanotechnology, University of Queensland, Australia

[4] National Imaging Facility, Centre for Advanced Imaging, University of Queensland, Australia

[5] School of Pharmacy and Medical Sciences, Griffith University, Australia

* Correspondence: Hang Thu Ta (h.ta@griffith.edu.au)

Corresponding author:

Hang Thu Ta, BEng, MSc, PhD

Associate Professor, School of Environment and Science, and Queensland Micro- and Nanotechnology, Griffith University, Nathan Campus, Brisbane QLD 4111, Australia

Honorary Associate Professor, Australian Institute for Bioengineering and Nanotechnology, University of Queensland, St Lucia, Brisbane QLD 4067, Australia

Office: +61 (7) 3735 5384

Email: h.ta@griffith.edu.au

Website: https://hangta.group/

https://experts.griffith.edu.au/27034-hang-ta

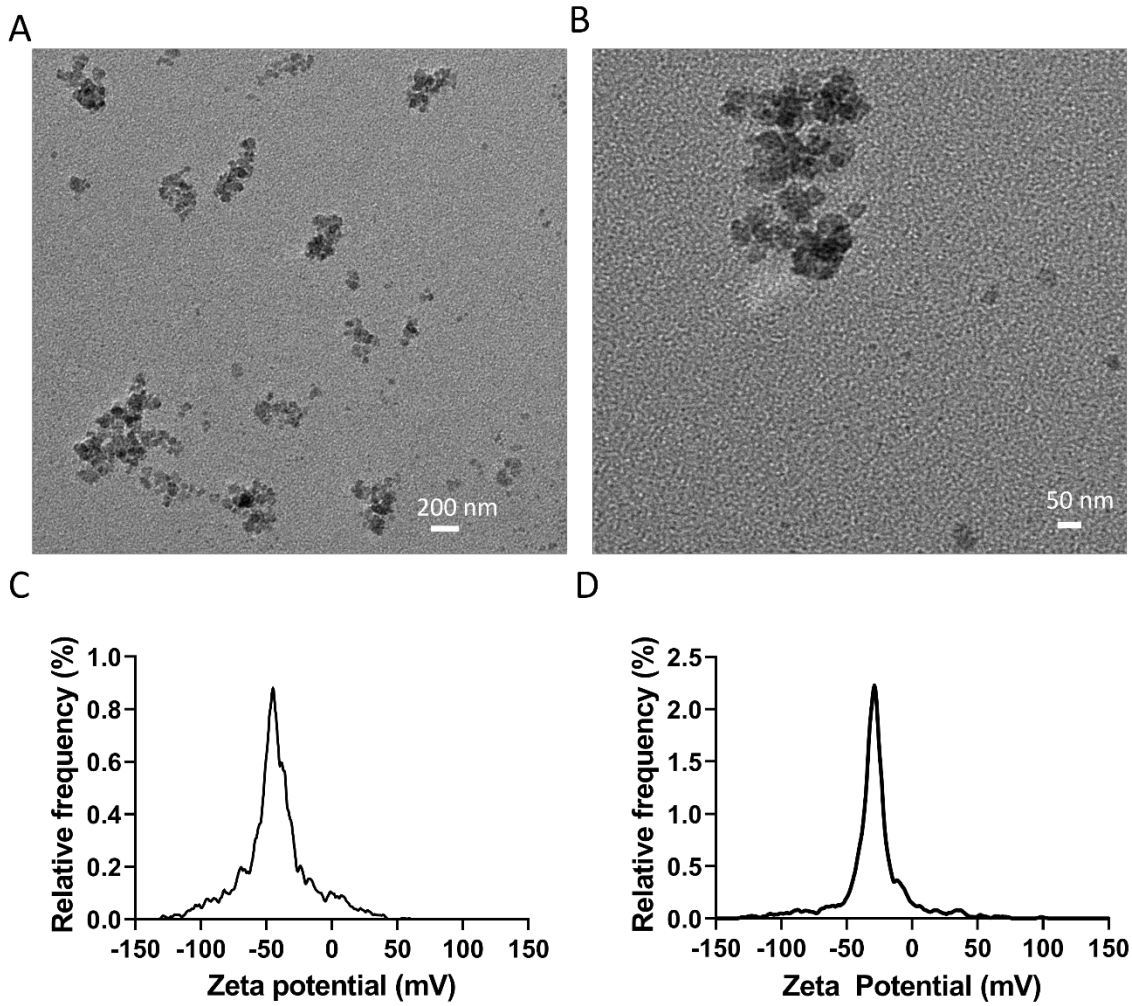

Figure S1. Characterisation of IONPs & AgIONPs. A & B) TEM images showing IONPs in clusters. **C)** Zeta potential peak of IONPs. **D)** Zeta potential of AgIONPs

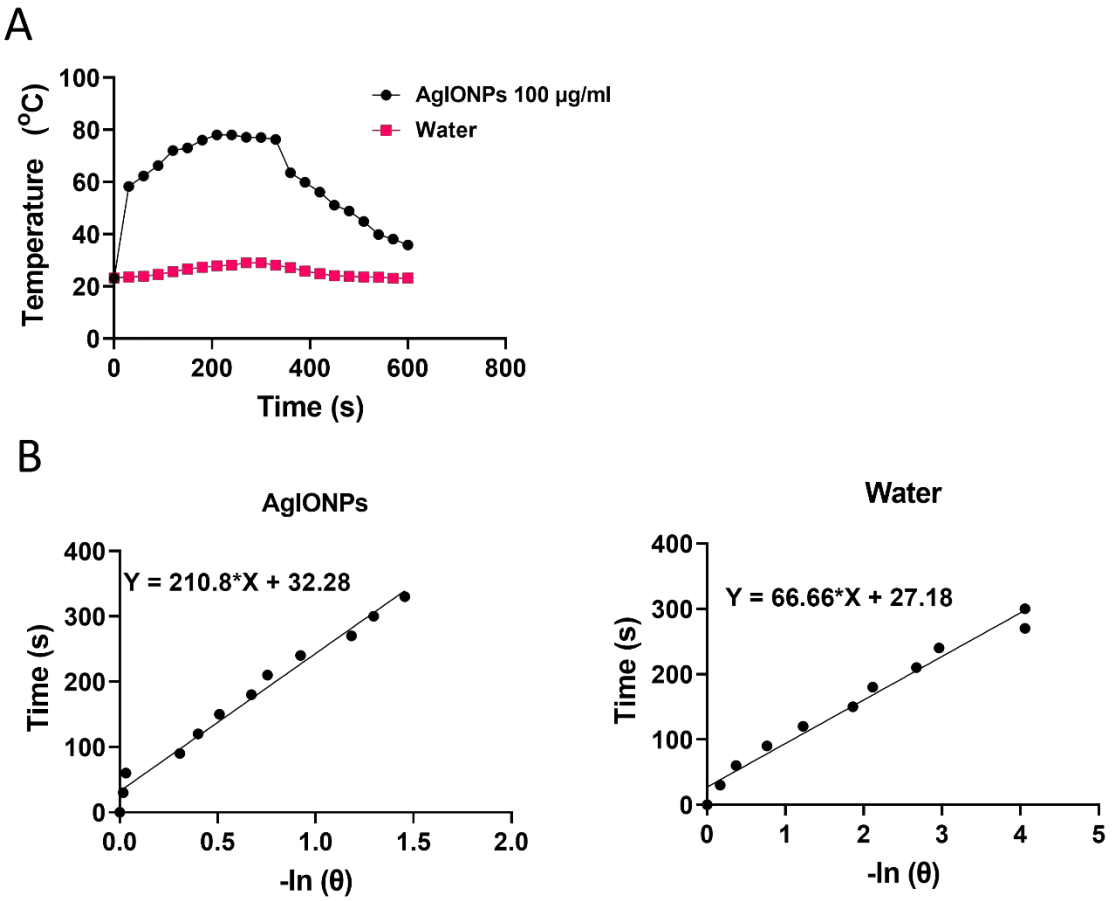

Figure S2. Photothermal conversion efficiency calculation. **A)** Temperature change at every 30 seconds for 300 seconds of AgIONPs (100 µg/ml) and water with NIR irradiation (808 nm, 1.5 W/cm^2). At the end of 300 seconds, the laser was shut off and temperature change was recorded for a further 300 seconds. **B)** Plot of -ln(Θ) vs time of the cooling period to calculate the photothermal conversion efficiency.

Photothermal conversion efficiency was calculated based on Qian et al [1] with the utilisation of **Equation 1** as detailed below:

$$\eta = \frac{hs\,(T_{max} - T_{surr}) - Q_{Dis}}{I(1 - 10^{-A_{808}})} \qquad \text{Equation 1}$$

h = heat transfer coefficient
s = surface area of the container
Tmax = maximum temperature obtained with laser irradiation
Tsurr = initial temperature before the laser irradiation
Q_{Dis} = heat absorbed by solvent and container
I = Intensity of the laser
A_{808} = Absorbance of NPs at 808 nm

hs value was obtained via a dimensionless parameter Θ and a sample system time constant which can be calculated by the following **Equation 2** and **3** respectively:

$$\Theta = \frac{T - T_{surr}}{T_{Max} - T_{Surr}}$$ Equation 2

$$t = -\tau_s \, ln\,(\Theta)$$ Equation 3

where $\boldsymbol{\tau}$s can be determined by obtaining the slope value of -ln(Θ) vs time (Figure S3B) from the cooling period of the observation. Based on this, we obtained $\boldsymbol{\tau}$s value for AgIONP and water as 210.8 and 66.66 respectively.

Subsequently, hs is obtained with Equation 4:

$$hs = \frac{m\,C}{\tau_s}$$ Equation 4

m = 0.1 g

C = 4.2 J/g℃.

Hence, hs value is calculated to be 0.002 W/°C, (T_{max} - T_{surr}) = 54 °C, Q_{Dis}= 0.006 W/°C, laser power = 0.48 W, Absorbance at 808 nm = 2.11 are substituted into **Equation 1** to obtain a photothermal conversion efficiency of **21.4** %.

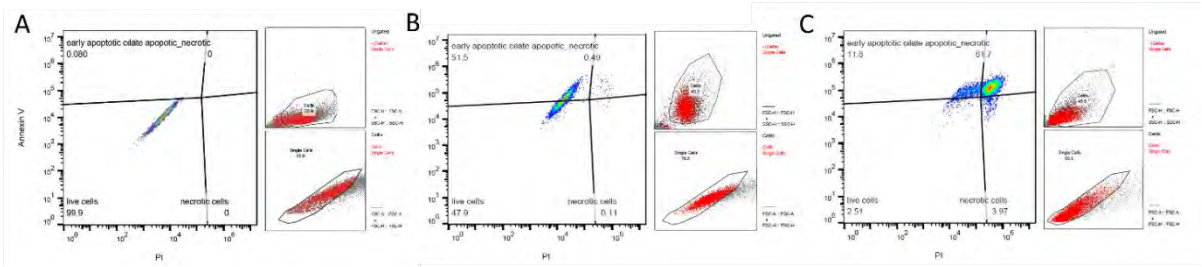

Figure S3. Flow cytometry analysis of U87MG cells to determine different population of apoptotic cells. **A)** untreated control, **B)** treated with 100 µg/ml of FA-AgIONPs **C)** NPs and laser irradiation at 1.5W/cm^2, 5 mins.

Table S1. Characterisation of NPs

NPs	Z-Average (nm)	PDI	Zeta potential (mV)
IONPs	58.3 ± 0.9	0.188 ± 0.017	-45.8 ± 1.1
AgIONPs	165.3 ± 0.2	0.060 ± 0.0133	-29.0 ± 2.2
FA-AgIONPs	175.6 ± 0.3	0.006 ± 0.022	-14.9 ± 2.8

Table S2. Different mass ratio of FA-PEG-SH conjugation to AgIONPs

FA: NPs	Size (nm)	PDI	Zeta potential (mV)
Control	165.3	0.09	-28 ± 1.2
1:50	165.6	0.091	-20 ±1
1:37.5	170.75	0.094	-15.9 ± 0.9
1:25	172.97	0.006	-13.4 ± 0.8
1:17.5	176.74	0.001	-12.2 ± 0.9
1:10	175.6	0.006	-8.6 ± 0.7

Table S3. Stability of different mass ratio of FA-PEG-SH conjugation to AgIONP in PBS

FA: NPs	Time in PBS (hrs)	Stability (%)	Size (nm)	PDI
1:10	1	99.4		
1:10	4	96.8	171.63	0.133
1:10	24	88.4	164.58	0.124
1:10	1 wk	72.6		
1:17.5	1	95.1		
1:17.5	4	93.5	172.05	0.061
1:17.5	24	92.3	164.54	0.078
1:17.5	1 wk	64		
1:25	1	99.99		
1:25	4	94.8	167.28	0.067
1:25	24	86.6	162.93	0.17
1:25	1 wk	74		
1:37.5	1	97.6		
	4	96.4	167.26	0.11
	24	76	166.5	0.049
	1 wk	70.5		
1:50	1	99.2		
	4	98.74	163.68	0.039
	24	92.5	163.32	0.044
	1 wk	72.5		

Table S4. Stability of optimised 1:25 mass ratio of FA-PEG-SH conjugated AgIONPs in PBS.

Time in PBS (hrs)	Stability (%)	Size (nm)	PDI
1 hr	99.99	168.9	0.06
4	94.8	167.28	0.067
24	86.6	162.93	0.17
1 wk	74	171.20	0.19

[1] X. Liu, B. Li, F. Fu, K. Xu, R. Zou, Q. Wang, B. Zhang, Z. Chen, J. Hu, *Dalton Transactions* **2014**, 43, 11709.